

Dissection of H α Emitters : Low- z Analogs of $z > 4$ Star-Forming Galaxies

Hyunjin Shim^{1,2} & Ranga-Ram Chary³

ABSTRACT

Strong H α Emitters (HAEs) dominate the $z \sim 4$ Lyman-break galaxy population. We have identified local analogs of these HAEs using the Sloan Digital Sky Survey (SDSS). At $z < 0.4$, only 0.04% of galaxies are classified as HAEs with H α equivalent widths ($\gtrsim 500 \text{ \AA}$) comparable to that of $z \sim 4$ HAEs. Local HAEs have lower stellar mass and lower ultraviolet (UV) luminosity than $z \sim 4$ HAEs, yet the H α -to-UV luminosity ratio as well as their specific star-formation rate is consistent with that of $z \sim 4$ HAEs indicating that they are scaled down versions of high- z star-forming galaxies. Compared to the previously studied local analogs of $z \sim 2$ Lyman break galaxies selected using rest-frame UV, local HAEs show similar UV luminosity surface density, weaker $D_n(4000)$ breaks, lower metallicity and lower stellar mass. This supports the idea that local HAEs are less evolved galaxies than the traditional Lyman break analogs. We are not able to constrain if the star-formation history in local HAEs is powered by mergers or by cosmological cold flow accretion. However, in the stacked spectrum, local HAEs show a strong HeII $\lambda 4686$ emission line suggesting a population of young ($< 10 \text{ Myr}$), hot, massive stars similar to that seen in some Wolf-Rayet galaxies. Low [NII]/[OIII] line flux ratios imply that local HAEs are inconsistent with being systems that host bright AGN. Instead, it is highly likely that local HAEs are galaxies with an elevated ionization parameter, either due to a high electron density or large escape fraction of hydrogen ionizing photons as in the case for Wolf-Rayet galaxies.

Subject headings: cosmology: observation – galaxies: evolution – galaxies: starburst – galaxies: low-redshift

1. Introduction

In attempts to understand the cosmic star formation history over cosmic time, most conventional approaches select high-redshift star-forming galaxies based on different unique signatures in their spectral energy distribution. Well-known examples are the Lyman-break in the ultraviolet (UV) continuum, Lyman- α emission line, the Balmer-break in evolved stellar populations and more

¹Department of Earth Science Education, Kyungpook National University, Korea; hjshim@knu.ac.kr

²Spitzer Science Center, California Institute of Technology, MS 220-6, Pasadena, CA 91125

³U.S. Planck Data Center, California Institute of Technology, MS 220-6, Pasadena, CA 91125

recently, the shape of the observed far-infrared spectral energy distribution which shows a peak between ~ 60 and $100\mu\text{m}$. The next step is to investigate their physical properties such as star formation rates, stellar mass and stellar populations using yardsticks calibrated in the local universe for which higher signal to noise and higher spatial resolution data are available, compared to the high-redshift galaxies considered. By studying the local counterparts of high-redshift galaxies, it is possible to understand the physical trigger for star-formation and its temporal evolution, and how physical parameters in the interstellar medium affect observables that trace the star formation activity.

One well known study is the investigation of local UV-luminous galaxies as analogs of high-redshift Lyman-break galaxies. Heckman et al.(2005) have studied the properties of FUV-luminous galaxies at $z \lesssim 0.3$ using the combination of Galaxy Evolution Explorer (GALEX) and Sloan Digital Sky Survey (SDSS) data. The FUV luminosities of the selected galaxies are greater than $2 \times 10^{10} L_{\odot}$, comparable to that of $z \sim 2 - 3$ Lyman break galaxies (LBGs). The number density of such UV-luminous galaxies (UVLGs) is 0.85 % of all galaxies at $0.0 < z < 0.3$ (Hoopes et al. 2007). Hoopes et al.(2007) have shown that the specific star formation rate of UVLGs is correlated with their UV surface brightness, and the subset of compact UVLGs with the highest UV surface brightness (i.e., $I_{FUV} > 10^9 L_{\odot} \text{kpc}^{-2}$; supercompact UVLGs) are likely to be the local counterparts to high-redshift LBGs in terms of their UV surface brightness, star formation rate, metallicity, and stellar mass.

These supercompact UVLGs, later denoted as Lyman break Analogs (LBAs), have been studied in detail in the radio (Basu-Zych et al. 2007) and infrared (Overzier et al. 2009; Overzier et al. 2011) which helps provide a window into high-redshift star forming environments in the local Universe. For example, high spatial resolution studies of the morphologies of LBAs show clear evidence of merger-induced star formation (Overzier et al. 2008, 2010). In contrast, the signatures of mergers are not visible in the rest-frame UV observation of high-redshift galaxies. Ravindranath et al. (2006) demonstrated that only $\sim 30\%$ of $z > 3$ galaxies show signatures of mergers. It is plausible that this derived fraction is a lower limit due to surface brightness dimming (Overzier et al. 2010). However, there is a theoretical suggestion that high-redshift star formation is preferentially governed by a supply of cold gas through cold flow accretion rather than merging (Dekel et al. 2009). The mechanism may not be valid in the local universe due to the fact that the halo masses are much larger and the gas gets shock heated before it falls within the virial radius of the halo. Thus, the ‘local counterparts’ of high-redshift star-forming galaxies may not necessarily have a similar source of gas supply as distant galaxies. However, their similarity in observable properties are useful for evaluating if the derived physical quantities for high redshift galaxies, such as star formation rates and dust obscuration are accurate. Thus, the key question is whether the UV-selected LBAs are accurate local analogs for high-redshift star-forming galaxies.

Recently, we have discovered that at least 70 % of spectroscopically confirmed Lyman-break galaxies at $3.8 < z < 5.0$ show a flux density excess in *Spitzer* $3.6\mu\text{m}$ over the stellar continuum, which is due to redshifted $\text{H}\alpha$ emission (Shim et al. 2011, $\text{H}\alpha$ Emitters; hereafter HAEs). The result

is striking for two reasons; one is that strong nebular emission lines do affect broad-band photometry and photometry-based SED fitting (e.g. Chary et al. 2005, Zackrisson et al. 2008, Capak et al. 2011, Schaerer & de Barros 2009), and two, high-redshift galaxies show strong H α emission which implies a star-formation rate that is as high, if not higher than that inferred from their large UV luminosities. The estimated H α equivalent widths (EWs) are in the range of 140 – 1700 Å, rarely seen in surveys of local galaxies. Despite the selection bias in favor of emission line sources that is associated with spectroscopic confirmation of Lyman-break galaxies, the value of 70 % is unusually high. It suggests that there is a physical reason for this ‘strong H α phase’ that was previously not known. The high H α -to-UV ratio and large H α EW compared to the ages of the stellar population therein suggest that at least 50 % of $z \sim 4$ HAEs prefer an extended star formation timescale rather than a burst-like, short (~ 100 Myr) timescale. Therefore, such extended star formation histories should be included in the selection criteria for local counterparts of high-redshift star-forming galaxies.

Large H α EW galaxies can be easily identified among local samples. In this paper, we selected local galaxies ($z < 0.4$) with H α EW > 500 Å from the Sloan Digital Sky Survey (SDSS). We use the measured properties of these local HAEs, to understand the properties of $z \gtrsim 4$ HAEs that dominate the high-redshift star-forming galaxy population. We investigate possible reasons for the origin of strong H α emission in star-forming galaxies (presence of active galactic nuclei, low metallicity, extended star formation histories, and dust extinction) by using spectroscopically derived values such as line indices and metallicity, as well as UV-to-IR flux ratios. A comparison between properties of HAEs and LBAs is discussed, and the implications of our improved understanding of local HAEs to high-redshift star formation is presented. Throughout this paper, we use a cosmology with $\Omega_M = 0.27$, $\Omega_\Lambda = 0.73$, and $H_0 = 71 \text{ km s}^{-1} \text{ Mpc}^{-1}$. All magnitudes mentioned are in AB mag, corrected for Galactic extinction using the Schlegel et al.(1998) dust map.

2. The Local Sample of H α Emitters

2.1. Local H α Emitters

We selected objects with H α EW larger than 500 Å from Sloan Digital Sky Survey (SDSS) Data Release 7, using the MPA-JHU value added catalog¹ (Kauffmann et al. 2003a; Brinchmann et al. 2004). After the H α EW cut, we inspected each object individually in the SDSS image and spectrum. Extragalactic HII regions, which reside in the spiral arms of large $z \sim 0$ galaxies, are discarded. Due to the limited fiber size used in SDSS spectroscopy (3'' diameter), the measured H α EW corresponds to the equivalent width in the central regions of an extended galaxy. Thus the galaxy-integrated H α EW may be different if the line to continuum ratio changes dramatically in the outer parts of a galaxy. To ensure that gradients in equivalent widths do not significantly affect

¹<http://www.mpa-garching.mpg.de/SDSS/DR7/>

our results, we excluded objects with half-light radii larger than $3''$ (using r_{50} in r -band; exponential disk fitting from SDSS pipeline). Finally, we are left with 299 galaxies ($\sim 0.04\%$) out of 818333 galaxies spectroscopically observed in SDSS DR7. We refer these galaxies as ‘local HAEs’.

As discussed above, the fiber spectra only sample the central regions for extended objects. Since it is possible that the stellar continuum may be less centrally concentrated compared to the line emission, aperture corrections are required as described in Brinchmann et al. (2004). Brinchmann et al.(2004) estimated the aperture correction of up to a factor of 10 to be applied to the star formation rates and stellar mass values in the MPA-JHU catalogs, based on the likelihood distribution function $P(\text{SFR}/L_i\text{—color})$. In order to further ensure that the line flux measurements and equivalent width measurements are robust, we convolved the SDSS spectrum with the band-passes used for photometry, and compared the magnitudes derived in this way with the observed broadband magnitudes. At redshifts greater than 0.05, the $\text{H}\alpha$ line falls within the Sloan i -band filter while at lower redshifts, the line would be in the Sloan r -band filter. As a result, aperture corrections based on either r or i -band photometry would take any variation in equivalent width outside the fiber into account. We found the median correction factor for the line flux estimates to be ~ 1.5 .

Table 1 lists the SDSS photo-object IDs, coordinates, $\text{H}\alpha$ flux and equivalent width, and other parameters for local HAEs. The $\text{H}\alpha$ flux and equivalent width are the observed values. The analysis such as the derivation of $\text{H}\alpha$ luminosity has been performed after applying aperture correction on the numbers presented in the Table 1

2.2. Ancillary Data Used

Most parameters used in this analysis are drawn either from MPA-JHU value added catalog and/or the SDSS pipeline. Stellar mass, metallicity, line fluxes and equivalent widths for significant emission lines, 4000 Å break $D_n(4000)$ in the MPA-JHU value added catalog are obtained through spectral and/or multi-wavelength photometry fitting. Here we briefly describe how each parameter is derived in the MPA-JHU value added catalogs.

Metallicities, i.e., the oxygen abundances, were derived following the method presented in Tremonti et al.(2004). All the most prominent emission lines ($[\text{OII}]$, $\text{H}\beta$, $[\text{OIII}]$, $\text{H}\alpha$, $[\text{NII}]$, $[\text{SII}]$) were fit simultaneously to $\sim 2 \times 10^5$ models for integrated galaxy spectra (Charlot & Longhetti 2001) with varying metallicity, ionization parameter, and dust-to-metal ratio. The median of the likelihood distribution of the metallicity was adopted as the metallicity of each galaxy. The stellar masses were derived based on the multi-wavelength photometry fitting, following the method described in Kauffmann et al.(2003a) and Salim et al.(2007). Template galaxy spectra were generated using Bruzual & Charlot (2003) population synthesis code, with metallicity range spanning $0.1 - 2 Z_\odot$ and stellar population age spanning 0.1 Gyr to the age of the universe. An exponentially decaying star formation history was assumed with random starbursts superimposed on the continuous star

formation. Internal reddening and attenuation due to the IGM are applied to the template galaxy spectra, and the resulting template spectra were convolved with SDSS passbands to produce broad-band photometry in each filter. After calculating χ^2 of the fit, probability distributions for each parameters, such as star formation rate, stellar masses, and dust attenuation were constructed. Rather than finding single best-fit template, the MPA-JHU value added catalog presents the median of the distribution of each parameter in order to avoid the degeneracies between parameters.

We have now added GALEX far- and near-ultraviolet (FUV/NUV) flux densities of local HAEs from GALEX Data Release 6. GALEX has a spatial resolution of $\sim 6''$. Using a cross-identification radius of $3''$, 266 HAEs among 299 ($\sim 90\%$) are observed in at least one GALEX band. After matching, each result was visually examined to make sure that FUV or NUV emission is from the local HAE itself, and not contaminated by nearby objects. The flux density limit differs depending on which GALEX survey the ultraviolet flux has been derived from - however on average, the flux density limits in the FUV (1500 \AA) and NUV (2300 \AA) are $5 \mu\text{Jy}$ and $4 \mu\text{Jy}$ respectively.

We also obtained mid-infrared (MIR; $3 - 22 \mu\text{m}$) photometry for local HAEs from the Wide-field Infrared Survey Explorer (WISE) preliminary data release (Wright et al. 2010). 95 of the galaxies ($95/299$, $\sim 30\%$) have coverage during the WISE preliminary survey period, among which 65 galaxies are detected in either WISE channel 3 ($12 \mu\text{m}$) or channel 4 ($22 \mu\text{m}$) with approximate flux density limits of $S_{12\mu\text{m}} > 1 \text{ mJy}$ and $S_{22\mu\text{m}} > 4.3 \text{ mJy}$ at the 5σ level. WISE channel 3 and channel 4 band fluxes are converted to total infrared luminosities using bolometric corrections derived from model infrared galaxy templates (Chary & Pope 2010).

3. Comparison with Other Galaxies

3.1. Comparison with $z \sim 4$ HAEs

Local HAEs are distributed at $0 < z < 0.4$, with more than half lying at $z < 0.1$ (Figure 1). Figure 2 shows how local HAEs and their $z \sim 4$ counterparts (Shim et al. 2011) compare with each other in terms of the physical properties of their stellar populations. In Figure 2a, we compare the $\text{H}\alpha$ and FUV luminosity of local HAEs, $z \sim 4$ HAEs and LBAs from Overzier et al. (2011). The $\text{H}\alpha/\text{FUV}$ luminosity ratio of both local and $z \sim 4$ HAEs are similar (~ 0.032) while the local LBAs show a ratio of ~ 0.0063 . The dotted line in Figure 2a is a linear fit to describe the correlation between $\text{H}\alpha$ luminosity and UV luminosity of local HAEs, with a slope value of 0.99. Since both $\text{H}\alpha$ and UV are star-formation tracers which are affected by age and dust obscuration in different ways, a slope close to unity indicates that both sets of galaxies display similar physical properties of the stellar population and ISM. However, local HAEs have $\text{H}\alpha$ luminosities and UV luminosities lower than that of $z \sim 4$ HAEs by nearly an order of magnitude, which means that the actual star formation rates of local HAEs are smaller than their high-redshift counterparts by a factor of ~ 10 (Figure 2b). It is however clear that $z \sim 4$ HAEs are scaled-up versions of local HAEs.

In Figure 2b, we compare the star-formation rates relative to the stellar mass of local HAEs, $z \sim 4$ HAEs and LBAs. The $H\alpha$ based star-formation rates are derived assuming a Salpeter IMF and a constant star-formation rate. The ratio of star-formation rate to stellar mass is referred to as the specific star-formation rate. Dotted diagonal lines in the figure show specific star-formation rates at different redshifts of star-forming main sequence galaxies based on the literature (Elbaz et al. 2007; Noeske et al. 2007; Daddi et al. 2007). Local HAEs show $H\alpha$ based star-formation rates that are almost a factor of 30 higher than typical star-forming galaxies of the same stellar mass, i.e. they show elevated specific star-formation rates which are comparable to that of $z \sim 4$ HAEs and merger-driven high-redshift submillimeter galaxies. The stellar mass range sampled by local HAEs is on average lower than that of $z \sim 4$ HAEs. Although, there is a significant overlap at $10^9 - 10^{10} M_{\odot}$; yet a dominant fraction ($\sim 65\%$) of local HAEs appear to be small galaxies with stellar mass smaller than $10^9 M_{\odot}$.

It is therefore clear that the $H\alpha$ $EW > 500\text{\AA}$ selection identifies local galaxies that are similar in their specific star-formation rates to large $H\alpha$ EW galaxies at $z \sim 4$ but with scaled down star-formation rates and stellar masses. Note that it is also possible that there could be $z \sim 4$ HAEs with $H\alpha$ EW less than 500\AA . However, since our selection for high redshift HAEs is based on the broad-band photometric excess in the Spitzer $3.6\mu\text{m}$ imaging data in the Great Observatories Origins Deep Survey fields (Shim et al. 2011) we are biased towards selecting the largest equivalent width objects. Such large EW objects are also being found in wide-field spectroscopic imaging surveys (Atek et al. 2011). Nevertheless, $\sim 70\%$ of spectroscopically selected $z \sim 4$ galaxies (most of which are initially classified as Lyman break galaxies) are observed to show a photometric excess, reflecting strong $H\alpha$ emission with $H\alpha$ $EW > 500\text{\AA}$.

3.2. Comparison with Local UV-selected Star-forming Galaxies

We next compare local HAEs with local analogs of $z \sim 2$ star-forming galaxies: UV luminous galaxies (UVLG) and Lyman break analogs (LBAs) which are a subset of UVLGs.

Contrary to the consistency between local HAEs and $z \sim 4$ HAEs, the local analogs of Lyman break galaxies (Heckman et al. 2005; Hoopes et al. 2007; Overzier et al. 2009) show significant differences with $z \sim 4$ HAEs in terms of $H\alpha$ EW . Lyman break analogs (LBAs) share a similar stellar mass range with $z \sim 4$ HAEs, but most of the LBAs have $H\alpha$ EW lower than 500\AA (Figure 3). While LBAs have been shown to have UV luminosity surface density consistent with that of Lyman break galaxies, their $H\alpha$ emission is significantly weaker than that of the $z \sim 4$ Lyman break galaxies. This implies that either the star formation history and/or the physical parameters related to star formation are likely different between LBAs and high-redshift Lyman break galaxies. Furthermore, the LBAs are thought to be more analogous to the $z \sim 2$ galaxy population where the $H\alpha$ EW s are correspondingly lower (Reddy et al. 2010, Erb et al. 2006).

In Figure 2a, LBAs lie consistently below the dotted line describing the $H\alpha$ -to-UV luminosity

ratio for HAEs. On average, the H α luminosity of LBAs is > 3 times lower than HAEs with the same UV luminosity. Since H α EW is closely tied to the age of the stellar population and the metallicity, it appears that the LBAs might have older, higher metallicity stellar populations than both local and $z \sim 4$ HAEs, a scenario we will investigate in greater detail in Section 5. Based on these observed differences, it appears that the LBAs are unlikely to be representative of typical star-forming galaxies at $z \sim 4$.

Figure 3 illustrates the distribution of H α EW and UV surface brightness of local HAEs and UVLGs ($L_{FUV} > 10^{10.3} L_{\odot}$). The UV surface brightness is estimated at 1530 Å, i.e., the central wavelength of GALEX FUV-band. The surface brightness is calculated by dividing one-half the rest-frame 1530 Å luminosity by the area of the galaxy encompassed within the half-light radius in the u -band ($I_{FUV} = L_{FUV}/2\pi r_{50,u}^2$; Hoopes et al. 2007). For the half-light radius in u -band, we used the radius from the seeing-corrected exponential model fit calculated by the SDSS pipeline which is consistent with the analysis of Hoopes et al.(2007). For galaxies larger than 2.2'' which would be resolved even in seeing limited images, the observed half-light radius was used instead of the seeing-corrected radius. There are only two overlapping objects between the samples of local HAEs and UVLGs. The SDSS object ids (photometric id) of these two are 587724199349387411 ($z = 0.287$) and 588013384341913605 ($z = 0.181$; Table 1). The two objects are marked as red points enclosed with large red circles with I_{FUV} values calculated using the technique outlined above. The triangles enclosed with larger triangles show the I_{FUV} values for these two objects in Hoopes et al. (2007), which are in excellent agreement with our values. Discrepancies in the derived FUV surface brightness originate from adopting different FUV magnitudes; GALEX Data Release 2 (used in Hoopes et al. 2007) magnitudes are superseded by GALEX Data Release 6 (used in our analysis).

The median H α EW of UVLGs is only ~ 100 Å, which is far less than the value used in the selection criteria of local HAEs (> 500 Å). The LBAs, since they have higher UV surface brightnesses, should thereby show higher specific SFR (Hoopes et al. 2007), and thus larger H α EW. The median H α EW of compact ($I_{FUV} > 10^9 L_{\odot} \text{ kpc}^{-2}$) UVLGs are indeed slightly larger than that of large ($I_{FUV} < 10^9 L_{\odot} \text{ kpc}^{-2}$) UVLGs (Figure 3), yet the correlation between UV surface brightness and H α EW of LBAs (compact UVLGs) is not significant. No such correlation can be seen in local HAEs. Remarkably, $\sim 50\%$ of local HAEs have UV surface brightness higher than $10^9 L_{\odot} \text{ kpc}^{-2}$, comparable with that of LBAs. This high UV surface brightness is mostly due to the small half-light radius of local HAEs rather than the UV luminosity itself. While UVLGs (thus LBAs) are defined as galaxies with L_{FUV} larger than $2 \times 10^{10} L_{\odot}$, the L_{FUV} distribution of local HAEs ranges between $5 \times 10^6 - 10^{11} L_{\odot}$.

Many local HAEs show compact morphologies despite their redshift distribution skewed towards lower redshift compared to UVLGs. The redshift distribution of UVLGs ranges between $z = 0.05 - 0.3$, while the redshift distribution of HAEs ranges between $z = 0.001 - 0.35$. As a result, the half-light radius of local HAEs is in general smaller than 5 kpc, while the half-light radius ($r_{50,u}$) ranges between 1 – 15 kpc for UVLGs. Because of this difference in $r_{50,u}$, the me-

dian UV surface brightness ($\langle I_{FUV} \rangle$) of local HAEs ($10^9 L_{\odot} \text{ kpc}^{-2}$) is higher than that of UVLGs ($10^8 L_{\odot} \text{ kpc}^{-2}$). This shows that there exists a significant number of local starbursts with specific star-formation rates similar to that of high-redshift star-forming galaxies but which are missed in samples that use the total UV luminosity as the primary selection criterion.

Despite the similarity in UV surface brightness, the spectral features appearing in the composite spectrum of LBAs and local HAEs are significantly different. Figure 4 shows a comparison between the composite spectrum of LBAs and local HAEs (top), as well as the comparison between the composite spectrum of local HAEs and a single Wolf-Rayet galaxy, IC3591 (bottom). The composite spectrum of local HAEs is an average stack of the 197 local HAEs which do not show any signs of Wolf-Rayet signatures such as the blue bump around HeII 4686 Å and/or HeII 4686 Å emission line with S/N greater than 3. Before stacking, each spectrum was normalized using the continuum flux at 4800 Å. The composite spectrum of LBAs is an average stacking of the 27 LBAs (Overzier et al. 2009) using the same method. The composite spectrum of local HAEs shows slightly bluer stellar continuum at 4000 – 6000 Å. When the optical stellar continuum is approximated using $F_{\lambda} \propto \lambda^{-\gamma}$, the slope γ for local HAEs is 3.9 while that for LBAs is 1.8, two times lower.² The composite spectrum of local HAEs also shows clear HeII 4686 Å emission, HeI 4471 Å and 4921 Å lines, and other forbidden lines such as [FeIII] 4658 Å, [ArIV] 4711 Å and 4740 Å lines. The [NII] emission at either 6548 Å or 6584 Å is relatively weak compared to H α , and [OIII] doublet at 5007 Å is strong compared to H β in the local HAEs. The physical properties of the galaxies will be further discussed through the location of local HAEs in the emission line diagnostics diagram (Baldwin et al. 1981) in Section 4.

3.3. Comparison with Wolf-Rayet Galaxies

We matched the same of 299 local HAEs with the catalog of previously studied Wolf-Rayet galaxies (Zhang et al. 2007; Brinchmann et al. 2008b). In total, 43 local HAEs ($\sim 14\%$) are identified as Wolf-Rayet galaxies. Wolf-Rayet galaxies are specifically marked in Table 1. Besides these 43, we found that another 59 local HAEs show HeII $\lambda 4686$ emission line at line $S/N > 3$ in their spectra, despite they are not matched with Wolf-Rayet galaxy catalogs. For the remaining HAEs, we were able to construct a composite spectrum as described above. At the bottom panel of Figure 4, we compare the composite spectrum of local HAEs (197 objects without Wolf-Rayet signature in individual spectrum; same as Figure 4a) with the spectrum of a Wolf-Rayet galaxy IC 3591 (Brinchmann et al. 2008b). The composite spectrum does not show the existence of a broad blue bump typical of Wolf-Rayet galaxies. However, the fact that some of the local HAEs are Wolf-Rayet galaxies and the existence of the HeII 4686 Å emission line in the composite spectrum suggests that the star formation environment in some local HAEs may be similar to that of Wolf-Rayet galaxies.

²The slope is determined for arbitrary F_{λ} unit, thus the numbers should be used for relative comparison only.

The origin of the HeII 4686 Å line is however unclear and has been discussed extensively in Thuan & Izotov (2005) and Shirazi & Brinchmann (2012). The former argue for radiative shocks while the latter present a range of scenarios including a population of hot, early type stars due to stellar rotation. The strength of HeII 4686 Å is known to be dependent on H β EW (Brinchmann et al. 2008b; Shirazi & Brinchmann 2012). IC3591, compared here, has an H β EW of 263 Å (H α EW = 1556 Å) thus it is one of the galaxies with the largest H β EWs among Wolf-Rayet galaxies. We do not find any significant evidence for the strength of H α emission in the local HAEs being a preferential identifier of Wolf-Rayet galaxies. However, it appears that local HAEs are intermediate in their properties between Wolf-Rayet galaxies and LBAs in terms of their emission line strengths as well as the strength of the intrinsic ionizing photon field which is responsible for exciting the aforementioned lines. We discuss this in quantitative detail in the next section.

4. HeII Emission Line

The HeII 1640 Å emission line has long been suggested as a direct probe for hot Population III stars at high redshifts due to its high ionization potential of 54.4 eV (e.g. Schaerer 2003). Previous observations of high-redshift galaxies have only provided upper limits on HeII 1640 Å (e.g. Dawson et al. 2007). As illustrated in Figure 4, the composite spectrum of local HAEs shows clear HeII 4686 Å. Moreover, some of the local HAEs (59 out of 305) show HeII 4686 Å emission line over $S/N \sim 3$ in their individual spectrum even though they are not classified as Wolf-Rayet galaxies by previous studies (e.g., Brinchmann et al. 2008b). We measured the HeII 4686 Å emission line flux for local HAEs, and estimated the HeII 1640 Å line flux using the intensity ratio between different transitions ($n = 4$ to $n = 3$ for HeII λ 4686, and $n = 3$ to $n = 2$ for HeII λ 1640) for case B recombination (e.g. Osterbrock & Ferland 2006). We estimated the emission line flux by subtracting the stellar continuum through a simple linear fit and fitting a single Gaussian to the residual emission. Except for the case of the stacked spectrum of the 197 local HAEs which were stacked, we used line flux measurements from SDSS MPA-JHU value-added catalog for H α since the measurements take into account the effect of stellar absorption.

Figure 5 shows the ratio between H α flux and HeII λ 1640 flux for the individual and stacked HAEs. We divided the 197 local HAEs into two bins of metallicity, based on the bimodal metallicity distribution illustrated in Figure 6. The size of each subsample is roughly the same (~ 100). The color-coded filled circles represent the ratio from the stacked spectrum for two subsamples, one at $Z \sim 0.002$ and the other at $Z \sim 0.01$. Different colors represent different ratios for the conversion from HeII λ 4686 to HeII λ 1640. A ratio of HeII λ 1640/HeII λ 4686 of 7.42 ($T = 20000K$, $N_e = 10^4\text{cm}^{-3}$) is shown in red, 6.79 ($T = 10000K$, $N_e = 10^6\text{cm}^{-3}$) in green, 6.56 ($T = 10000K$, $N_e = 10^4\text{cm}^{-3}$) in cyan, and 5.90 ($T = 5000K$, $N_e = 10^4\text{cm}^{-3}$) in blue (Osterbrock & Ferland 2006). Overplotted are the expected H α /HeII λ 1640 ratio from the Starburst99 population synthesis model for a range of stellar initial mass functions and metallicity (Leitherer et al. 1999, Schaerer 2003).

As the different color-coded circles suggest, the observed $H\alpha/HeII$ ratios are not highly susceptible to variations in the physical parameters for HII regions such as temperature and/or electron density. A change in temperatures and/or electron density produces only a 50% change in the $H\alpha/HeII$ ratio. The effect of the initial mass function, including the mass range and the faint-end slope, is also limited to a factor of 2 – 3. The observed $H\alpha/HeII$ ratio for local HAEs is consistent with the expectation based on the Salpeter IMF with mass range of $1 - 200 M_{\odot}$ although the scatter in the points is large enough that a range of IMFs would be consistent with the data as shown by the gray filled region in Figure 5.

The two most dominant factors that result in a wide range of $H\alpha/HeII$ ratios are metallicity and star-formation history. As has been discussed in Schaerer (2003), metallicity strongly affects the ratio of Hydrogen to Helium ionizing photons output due to the increase in the effective stellar temperatures with decreasing metallicity. Thus, as metallicity decreases, the stellar population synthesis models result in a higher rate of Hydrogen ionizing photons produced relative to the number of Helium ionizing photons, which translates to an increasing $H\alpha/HeII \lambda 1640$ ratio. However, due to the short lifetimes of very massive, or hot Wolf-Rayet type stars that are responsible for the Helium ionizing photons, after 5 Myrs from the onset of star-formation, the HeII intensity drops while $H\alpha$ still remains elevated due to the existence of late B and A stars. This implies that $H\alpha/HeII \lambda 1640$ ratio increases at ages longer than 5 Myr relative to ages below 5 Myr.

Local HAEs span a range of metallicities as well as a range of HeII line strengths. The direct detection of HeII in the majority of local HAEs as well as the stacked detection of HeII in the HAEs which do not show HeII in their individual spectra implies that the HAEs harbor a very young stellar population. It is challenging to constrain the age of the stellar population very precisely due to the absence of obvious age indicators such as the 4000 Å break (See Section 5.2). For population synthesis models with continuous star-formation, the $H\alpha/HeII \lambda 1640$ ratio would be ~ 12 . Since $>90\%$ of local HAEs are above that ratio, the implied age of the stellar population in these galaxies must be less than 10 Myr strongly suggestive of local HAEs being powered by short bursts. The morphologies of these galaxies are however ambiguous in seeing-limited ground-based Sloan data. Space based data is required to assess if obvious signs of mergers are present in these objects.

Since we have demonstrated that local HAEs are analogs of $z \sim 4$ HAEs, we can estimate the HeII $\lambda 1640$ emission line flux from the $H\alpha$ line flux of $z \sim 4$ HAEs, and assess the feasibility of detecting the HeII $\lambda 1640$ emission line in the spectra of high-redshift sources. Using the $H\alpha/HeII$ ratio of ~ 50 (values measured in the stacked spectrum of low-metallicity local HAEs) and the median $H\alpha$ luminosity of $10^{43} \text{ erg s}^{-1}$ (Shim et al. 2011), the HeII $\lambda 1640$ line flux of $z \sim 4$ HAEs is expected to be $1.6 \times 10^{-18} \text{ erg s}^{-1} \text{ cm}^{-2}$. This is comparable but slightly lower than the HeII upper limits of Ly α emitters at $z \sim 4$ ($< 2 \times 10^{-18} \text{ erg s}^{-1} \text{ cm}^{-2}$; Dawson et al. 2007). However, it should be noted that the relationship between Ly α emitters and $H\alpha$ emitters is currently ambiguous. The $H\alpha$ emitters in Shim et al. (2011) are typical spectroscopically confirmed LBGs while the LAEs are preferentially lower mass systems. Therefore to detect the HeII $\lambda 1640$ emission line in $z > 4$ HAEs, future observations should aim to achieve line flux limits down to $5\sigma \sim 10^{-18} \text{ erg s}^{-1} \text{ cm}^{-2}$.

5. Properties of Local HAEs: Origins of Strong H α Emission

In Shim et al. (2011), we presented several possible reasons for the origin of unusually strong H α emission in the $z \sim 4$ HAEs, especially compared to other star-formation tracers such as the UV continuum. The possible factors that drive strong H α emission in high- z HAEs are: (1) extinction properties which are different with that of local starbursts (i.e., extinction curve steeper in UV), (2) young stellar population ages and star formation history, (3) low metallicity, and (4) a stellar initial mass function with an overabundance of massive stars. AGN were ruled out as a plausible explanation based on the non-detection of the $z \sim 4$ HAEs in the deep *Chandra* X-ray data. In the previous section, we had investigated the effect of stellar initial mass function. In this section, we investigate each of these possible scenarios for the origin of strong H α emission in local HAEs using the diagnostic properties of SDSS spectroscopy and UV-to-MIR photometry.

5.1. Low Metallicity

Figure 6 shows gas-phase metallicities ($12 + \log[O/H]$) and stellar masses of local HAEs from the MPA-JHU value added catalog for SDSS DR7. The metallicity distribution of local HAEs is clearly bimodal, one peak at $12 + \log[O/H] \sim 8.6$ and another peak at $12 + \log[O/H] \sim 8.0$. Half of the local HAEs are located at the low end of the stellar mass distribution ($M_* < 10^9 M_\odot$) and the low end of the metallicity distribution ($12 + \log[O/H] < 8.3$). This is different than the case for UVLGs (Hoopes et al. 2007). Almost all UVLGs are more massive than $10^9 M_\odot$ and have metallicity $12 + \log[O/H] > 8.3$. The most metal-rich UVLGs are almost super-solar metallicity. The higher metallicity of UVLGs, the higher masses compared to local HAEs and the absence of HeII in the spectra of UVLGs suggests that UVLGs are likely to be at a later stage of their star-formation history compared to HAEs.

The [OIII]/H α ratios of local HAEs do not appear to correlate with H α equivalent widths with a median line flux ratio of [OIII]/H $\alpha \sim 1.7$. Thus it is difficult to assess the connection between the gas-phase metallicity and the H α equivalent width. However, there is a clear trend where the lower metallicity systems appear to show a factor of 2 weaker [OIII] line flux corresponding to their H α line flux than the highest metallicity systems in the sample.

The low metallicity of local HAEs is also reflected in their [NII] $\lambda 6584$ /H α ratios, i.e., local HAEs show weak [NII] emission compared to H α . The median value of the observed [NII] $\lambda 6584$ /H α is ~ 0.08 , far less than the conventional [NII] $\lambda 6584$ /H $\alpha = 0.3$ for local star-forming galaxies (Gallego 1997). This places local HAEs well to the left of the line that divides starbursts and active galactic nuclei in the BPT diagram (Baldwin et al. 1981; Kauffmann et al. 2003b; Kewley et al. 2001), eliminating the possibility of the strong H α emission arising due to the presence of AGN. Figure 7 shows the location of local HAEs in the [OIII]5007/H β vs. [NII]6584/H α diagram. The location of the local HAE population in the BPT diagram partly depends on the gas-phase metallicity ($12 + \log[O/H]$), i.e., galaxies with lower metallicity show even less [NII]/H α ratio than galaxies

with higher metallicity (the different symbols of different colors trace the metallicity). Also shown for comparison are the location of Wolf-Rayet galaxies (Brinchmann et al. 2008b) and UVLGs (Hoopes et al. 2007) in the BPT diagram. Significant numbers of either Wolf-Rayet galaxies or UVLGs are classified as AGN-dominated systems, while most of Wolf-Rayet galaxies and/or UVLGs show higher $[\text{NII}]/\text{H}\alpha$ compared to local HAEs. Again as in Figure 6, the BPT diagram suggests that UVLGs, as well as Wolf-Rayet galaxies in general, are on average more evolved than local HAEs.

Another interesting point in Figure 7 is that local HAEs lie at the highest boundary of the entire local galaxy population showing the highest $[\text{OIII}]/\text{H}\beta$ ratios. It means that there exists a non-negligible offset between the median ridge line of $[\text{OIII}]/\text{H}\beta$ ratio for local galaxies and that of local HAEs (~ 1.6 in $[\text{OIII}]/\text{H}\beta$ line flux; Kewley & Dopita 2002). This offset is also reported for star-forming galaxies at $z > 2$ (Erb et al. 2006). Brinchmann et al.(2008a) suggest that this offset from the BPT ridge line is closely related to the amount of star formation, it being roughly proportional to the $\text{H}\alpha$ EW. High-redshift galaxies lying well above the ridge line are producing unusually large amounts of stars compared to their stellar mass, i.e., showing larger specific SFR, and this displacement can be achieved by increasing the ionization parameter (the ratio of the volume densities of ionizing photons and particles). Again, the increase of the ionization parameter depends on the ratio of ionizing photons, electron densities, and the geometry of HII regions which determines whether the HII regions are density-bound or ionization-bound: Brinchmann et al.(2008a) suggest higher electron densities and larger escape fraction of hydrogen ionizing photons as two major reasons for this offset in the BPT diagram. These can be also applicable to local HAEs, considering that local HAEs show a clear displacement in the BPT diagram comparable to other $z > 2$ star-forming galaxies. Thus, local HAEs appear to be excellent laboratories for the study of high- z star-forming environments and a measure of the ionizing photon flux from these objects would validate the origin of the unusual $[\text{OIII}]/\text{H}\beta$ ratios.

5.2. Star Formation History

In Shim et al.(2011), we demonstrated that the most dominant factor that drives the ‘strong $\text{H}\alpha$ phase’ is the star formation history of high- z star-forming galaxies. The ubiquity of strong $\text{H}\alpha$ emission and the evolved stellar population ages indicate that $z \sim 4$ star-forming galaxies appear to display continuous star formation histories rather than burst-like star formation. At $z \sim 4$, the interpretation corroborates a star formation mechanism that is powered by a continuous gas supply such as cold gas accretion from the filaments into massive halos. Short timescale events such as mergers would be stochastic and would suggest a strong $\text{H}\alpha$ emitting phase for only 10% of the galaxies.

In order to study the ages of the stellar population in local HAEs we compare the strength of the 4000 Å break, $D_n(4000)$, of these galaxies and UVLGs in Figure 8. Local HAEs sample a broad range of stellar masses covering $10^6 - 10^{10} M_\odot$, a broad range of FUV luminosity covering

$10^8 - 10^{11} L_{\odot}$, yet in terms of $D_n(4000)$, local HAEs are a relatively homogeneous population with $D_n(4000) < 1.0$. There is no correlation between $D_n(4000)$ and stellar mass or FUV luminosity. On the other hand, there is a positive correlation between $D_n(4000)$ and the stellar mass of UVLGs: older UVLGs appear to be more massive. UVLGs also appear to be in the middle of the range in the $D_n(4000)$ - M_* properties compared to Wolf-Rayet galaxies and HAEs.

Wolf-Rayet galaxies appear to show properties between those of HAEs and UVLGs. The $D_n(4000)$ of Wolf-Rayet galaxies is not as homogeneously small as HAEs. Furthermore, Wolf-Rayet galaxies are more massive than HAEs but less massive than UVLGs. Wolf-Rayet galaxies therefore appear to be older than HAEs of the same UV luminosity based on the strength of their 4000Å break but are younger than the majority of UVLGs. The composite spectrum of HAEs do show emission lines observed in Wolf-Rayet galaxies, such as Helium recombination lines which suggests some similarity in their ionizing photon field. The consistent FUV luminosity (Figure 8a), galaxy size (Figure 8b), and thus FUV surface brightness between the two also suggests the hypothesis that Wolf-Rayet galaxies and HAEs share similar interstellar medium condition, that enables high ionization parameter – higher electron densities, higher temperature, and a large escape fraction for hydrogen ionizing photons. Since the $D_n(4000)$ features arises due to absorption lines from ionized metals, the difference in $D_n(4000)$ between two populations suggests the possibility that HAEs are at an earlier lower metallicity stage of evolution than Wolf-Rayet galaxies.

5.3. Dust Obscuration in Local HAEs

In this subsection, we present and compare several different extinction indicators of local HAEs, constrain their extinction properties and thereby their true star-formation rate. We also assess the possible implications for the shape of the differential extinction as a function of wavelength.

5.3.1. Extinction Indicators

The first observable extinction indicator is the UV spectral slope β . β is derived based on the assumption that the spectrum of star-forming galaxies in the UV wavelength range are well described by a power-law ($f_{\lambda} \propto \lambda^{\beta}$). We assumed that this power-law approximation is applicable to the rest-frame wavelength range of $1500/(1+z)\text{Å} - 2300/(1+z)\text{Å}$, covered by the GALEX FUV and NUV bands. Then we converted the ($FUV - NUV$) color to a spectral slope β using the following relation.

$$\beta_{FUV-NUV} = (m_{FUV} - m_{NUV})/0.464 - 2.0 \tag{1}$$

m_{FUV} and m_{NUV} indicate the GALEX magnitudes in the FUV- and NUV-band corrected for Galactic extinction. The low S/N of the local HAEs in the GALEX FUV and NUV bands

propagates into the derived β . The derived $\beta_{FUV-NUV}$ is highly uncertain in most cases; 40 % of all objects have uncertainty higher than 0.2 in β .

The above assumption is accurate for objects with $z < 0.1$. However, for objects at $z > 0.1$, the Ly α emission line may contaminate the observed flux density in the GALEX FUV band which makes the broadband colors bluer and induces some uncertainty in β . For standard Case B recombination, the Ly α to H α line ratio is a factor of ~ 10 . We estimate that in the most extreme case, this would bias the FUV flux blueward by 20% and thereby affect the UV slope β by 0.4. We have not applied this correction because we do not know the true strength of the Ly α line in these sources and due to the fact that the effect of GALEX photometric uncertainty itself on β values is typically larger. Furthermore, the comparison with UVLGs and LBAs is more straightforward since those studies chose not to apply the correction as well.

The next extinction indicator is the flux ratio between Hydrogen recombination lines that traces the different extinction at the wavelengths corresponding to the lines. Here, we present the Balmer line ratio $F_{H\alpha}/F_{H\beta}$ as the extinction indicator. Following Calzetti et al. (2000), the color excess of the nebular gas, $E(B - V)_{gas}$, is calculated by comparing the observed Balmer line ratios with the intrinsic (i.e., unobscured) Balmer line ratios.

$$E(B - V)_{gas} = \frac{2.5}{k(\lambda_1) - k(\lambda_2)} \log_{10} \frac{F_i^{\lambda_1}/F_i^{\lambda_2}}{F_o^{\lambda_1}/F_o^{\lambda_2}} \quad (2)$$

Here, $F_i^{\lambda_1}/F_i^{\lambda_2}$ is the intrinsic line ratio, $F_o^{\lambda_1}/F_o^{\lambda_2}$ is the observed line ratio, and $k(\lambda)$ is an extinction value at the corresponding wavelength described by the applied extinction curve. Based on the case-B recombination at $T = 10^4$ K (Osterbrock & Ferland 2006), the intrinsic Balmer line ratio is $F_{H\alpha}/F_{H\beta} = 2.87$.

Finally, the ratio between IR luminosity and UV luminosity can be used as a third extinction indicator, assuming that the IR luminosity represents the entire unobscured stellar radiation. We derived IR luminosities of local HAEs using the WISE photometry in channel 3 and 4 ($12\mu\text{m}$ and $22\mu\text{m}$ respectively). By matching the coordinates of local HAEs to the WISE preliminary data release catalog (Wright et al. 2010), we found 65 objects with robust counterparts at a flux density level higher than 0.28 mJy at $12\mu\text{m}$ and 1.9 mJy at $22\mu\text{m}$. These objects do not have nearby neighbors within $3''$ that could possibly contaminate the MIR flux density. We used IR spectral energy distribution templates of IR galaxies with different IR luminosities (Chary & Pope 2010): each IR luminosity template was redshifted to the corresponding redshift of the object and the template that best explains the observed $12\mu\text{m}$ and $22\mu\text{m}$ flux density was determined, while the IR luminosity of the object was derived to be the IR luminosity associated with the best-fit template. IR luminosity of local HAEs ranges between $1.4 \times 10^8 L_{\odot}$ and $7.6 \times 10^{11} L_{\odot}$. We compared L_{IR} with L_{UV} , i.e., λL_{λ} at 1530 \AA as defined in the previous section, and used L_{IR}/L_{UV} as an extinction indicator.

The results for dust extinction using these three techniques is described in the next section.

5.3.2. Extinction Curve Difference in UV-wavelengths

Figure 9 illustrates the comparison between the three extinction indicators for local HAEs and LBAs. Figure 9a shows that there exists a positive correlation between UV slope β and $F_{H\alpha}/F_{H\beta}$, which is naturally expected from the fact that both quantities are providing independent measures of obscuration. However, the relationship between UV slope β and $F_{H\alpha}/F_{H\beta}$ for local HAEs and LBAs are different, i.e., for the same β , the flux ratio $F_{H\alpha}/F_{H\beta}$ is higher for LBAs than the case of HAEs. One possibility is that the ISM temperature in LBAs and HAEs is different, with the latter having higher gas temperatures which affects the recombination rate by a factor of 1.3. This would be consistent with the higher ultraviolet surface density seen in the HAEs compared to LBAs.

The alternate interpretation is this is a result of dust extinction. For a fixed $\beta_{FUV-NUV}$, LBAs show larger dust extinction than HAEs, which implies that the UV dust extinction curve is steeper in HAEs than in LBAs. This is more consistent with the extinction curve seen in the Small Magellanic Cloud (SMC) which due to its low metallicity is thought to have an overabundance of large grains relative to small grains (Weingartner & Draine 2001).

This possible difference in the shape of the dust extinction curve especially in the UV wavelength range has already been suggested in the study of $z \sim 4$ HAEs (Shim et al. 2011). Figure 9b shows the relationship between H α line-to-UV continuum ratio and UV slope β for local HAEs, in comparison with their high-redshift counterparts ($z \sim 4$ HAEs) and LBAs. For comparison, the figure also shows three lines indicating the starburst extinction law (Calzetti 2000), LMC extinction law (Fitzpatrick 1986), and SMC extinction law (Prevot 1984). The extinction laws that have a steeper curve at UV wavelengths (LMC, SMC) show higher H α -to-UV ratio compared to less steep extinction law (SB). The y -intercepts in these model lines depend on the assumed star formation history and the stellar population age of the galaxy while only the slope of the lines depend on the extinction law (See Shim et al. 2011). Higher-redshift HAEs have higher H α -to-UV ratio than local counterparts, implying that these are closer to continuously star-forming galaxies. Despite the y -intercept difference, HAEs at different redshifts show slopes in the H α -UV ratio vs. β relation which are consistent despite the large scatter. On the other hand, LBAs appear to have a slope that is completely different in the H α -UV ratio vs. β plane indicating that not only do they have distinct extinction properties to HAEs but also different star-formation histories.

Finally in Figures 9c, we present the IR-to-UV luminosity ratio for local HAEs. Since HAEs appear to be young galaxies while LBAs are relatively evolved galaxies, the IR-to-UV ratio of LBAs are expected to be smaller than that of HAEs since the fraction of stellar radiation that is absorbed by dust and re-radiated in the IR decreases as the galaxy evolves. The observed relation between the IR-to-UV ratio and UV spectral slope β for local HAEs lie above the expected line for local star-forming galaxies (Meurer et al. 1999) or that of LBAs, confirming the idea that young HAEs

have stronger intrinsic UV radiation fields and thereby emit more strongly in the IR. Still, the uncertainties related to the derivation of L_{IR} and $\beta_{FUV-NUV}$ is large. The addition of far-infrared continuum flux is needed to reduce the uncertainties in L_{IR} . To constrain the extinction curve shape in UV wavelengths in more detail, the accuracy in $\beta_{FUV-NUV}$ should also be improved with higher precision UV spectrophotometry which disentangles the contribution of the Ly- α line to the broadband photometry.

6. Summary

In this paper, we have studied the extremely rare, local analogs of $z \sim 4$ star-forming galaxies from SDSS DR7. It has recently been demonstrated in Shim et al. (2011) that 70% of $z \sim 4$ galaxies have strong H α equivalent widths and are H α emitters (HAEs). Therefore, unlike previous studies which selected local analogs based solely on their UV properties, we used the criterion H α EW $> 500 \text{ \AA}$ to select among the local galaxy population. At $z < 0.4$, the number fraction of such strong HAEs is only 0.04%. Local HAEs are less luminous by an order of magnitude in both H α and UV luminosities compared to $z \sim 4$ HAEs. However, the H α -to-UV luminosity ratio as well as the specific star-formation rates of local HAEs are very similar to those of high redshift HAEs. This supports the argument that local HAEs are scaled down versions of $z \sim 4$ star-forming galaxies.

In contrast, previously studied UV-selected local analogs of high-redshift Lyman-break galaxies, the Lyman-break analogs, are distinct in their physical properties from HAEs at any redshift. The UV-selected analogs show a factor of 5 lower H α EW, higher metallicity and higher stellar mass than the HAEs. At least 50% of local HAEs show comparably high FUV surface brightness as that of Lyman break galaxies and Lyman break analogs. However, the FUV surface brightness does not appear to depend on H α EW. Unlike the Lyman break analogs, the composite spectrum of local HAEs shows strong, but narrow Helium lines that are observed in Wolf-Rayet galaxies, raising the possibility that the properties of the star forming environment in local HAEs overlap with those of Wolf-Rayet galaxies.

As in the case of $z \sim 4$ HAEs, the strong H α emission in local HAEs can be attributed to a young stellar population with a large number of massive stars. 50% of local HAEs show low metallicity of $12 + \log[\text{O}/\text{H}] \sim 8.0$, close to $\sim 0.1 Z_{\odot}$ which is less than that of the UV-selected Lyman break analogs. This is consistent with the fact that HAEs are less massive by at least an order of magnitude than the Lyman break analogs. The low metallicities are also reflected in their low observed [NII]/H α ratio. The low [NII]/H α ratio, as well as high [OIII]/H β ratio, indicate that local HAEs are not contaminated by AGN-dominated systems. Moreover, the strong [OIII] emission that displaces local HAEs from the ridge line of BPT diagram can be explained by a high ionization parameter, which requires either higher electron densities and/or large escape fraction of hydrogen ionizing photons. If the large escape fraction is demonstrated through observational data, HAEs could be the clue to understanding the reionization of the intergalactic medium at high redshift.

Most HAEs are unusually young with $D_n(4000) < 1$. This is one of the largest differences between the properties of HAEs and Wolf-Rayet galaxies; the latter predominantly showing $D_n(4000) > 1$ suggesting a more evolved stellar population. Due to their small $D_n(4000)$, it is therefore difficult to constrain whether local HAEs follow a continuous star formation history or burst-like star formation history. The extinction indicator $H\alpha/H\beta$ of local HAEs suggests that HAEs display an extinction curve steeper than normal star-forming galaxies and more similar to that of the Small Magellanic Cloud. The origin of this difference in extinction curve is not clear with the most likely reason being the lower metallicities in these galaxies.

REFERENCES

- Allen, D. A. 1976, MNRAS, 174, 29
- Atek, H. et al. ApJ, 743, 121
- Baldwin, J. A., Phillips, M. M., & Terlevich, R. 1981, PASP, 93, 5
- Basu-Zych, A. R. et al. 2007, ApJS, 173, 457
- Brinchmann, J. et al. 2004, MNRAS, 351, 1151
- Brinchmann, J., Pettini, M., & Charlot, S. 2008, MNRAS, 385, 769
- Bruzual, G. & Charlot, S. 2003, MNRAS, 344, 1000
- Calzetti, D., Armus, L., Bohlin, R. C., Kinney, A. L., Koornneef, J., Storchi-Bergmann, T. 2000, ApJ, 533, 682
- Capak, P. et al. 2011, ApJ, 730, 68
- Charlot, S. & Loghetti, M. 2001, MNRAS, 323, 887
- Chary, R.-R. 2005, Stern, D., Eisenhardt, P. 2005, ApJL, 635, 5
- Chary, R.-R., & Pope, A. 2010 (arXiv:1003.1731)
- Coppin, K. E. K., 2009, MNRAS, 395, 1905
- Daddi, E. et al. 2007, ApJ, 670, 156
- Daddi, E. et al. 2009, ApJ, 694, 1517
- Dawson, S., et al., 2007, 671, 1227
- Dekel, A. et al. 2009, Nature, 457, 451
- Elbaz, D. et al. 2007, A&A, 468, 33

- Erb, D. K., Steidel, C. C., Shapley, A. E., Pettini, M., Reddy, N. A., & Adelberger, K. L. 2006, ApJ, 647, 128
- Fitzpatrick, E. L. 1986, AJ, 92, 1068
- Gallego, J., Zamorano, J., Rego, M., & Vitores, A. G. 1997, ApJ, 475, 502
- Heckman, T. M. et al. 2005, ApJL, 619, 35
- Hoopes, C. G. et al. 2007, ApJS, 173, 441
- Kauffmann, G. et al. 2003, MNRAS, 341, 33
- Kauffmann, G. et al. 2003, MNRAS, 346, 1055
- Kennicutt, R. C. 1998, ARA&A, 36, 189
- Kewley, L. J., Heisler, C. A., & Dopita, M. A. 2001, ApJS, 132
- Kewley, L. J. & Dopita, M. A., 2002, ApJS, 142, 35
- Leitherer, C., et al., 1999, ApJS, 123, 3
- Meurer, G. R., Heckman, T. M., & Calzetti, D. 1999, ApJ, 521, 64
- Noeske, K. G. et al. 2007, ApJL, 660, 47
- Osterbrock, D. & Ferland, G. 2006, *Astrophysics of Gaseous Nebulae and Active Galactic Nuclei*, 2nd. e.d., University Science Books
- Overzier, R. A. et al. 2008, ApJ, 677, 37
- Overzier, R. A. et al. 2009, ApJ, 706, 203
- Overzier, R. A. et al. 2010, ApJ, 710, 979
- Overzier, R. A. et al. 2011, ApJL, 726, 7
- Prévot, M. L., Lequeux, J., Prévot, L., Maurice, E., & Rocca-Volmerange, B. 1984, A&A, 132, 389
- Ravindranath, S. et al. 2006, ApJ, 652, 963
- Reddy, N. A., Erb, D. K., Pettini, M., Steidel, C. C., & Shapley, A. E. 2010, ApJ, 712, 1070
- Salim, S. et al. 2007, ApJS, 173, 267
- Schlegel, D. J., Finkbeiner, D. P., & Davis, M. 1998, ApJ, 500, 525
- Schaerer, D. 2003, A&A, 397, 527

- Schaerer, D. & de Barros, S. 2009, *A&A*, 502, 423
- Schinnerer, E. et al. 2008, *ApJL*, 689, 5
- Shim, H. et al. 2011, *ApJ*, 738, 69
- Shirazi, M. & Brinchmann, J. 2012, *MNRAS*, 421, 1043
- Tremonti, C. A. et al. 2004, *ApJ*, 613, 898
- Thuan, T. X., & Izotov, Y. I. 2005, *ApJS*, 161, 240
- Weingartner, J. C. & Draine, B. T. 2001, *ApJ*, 548, 296
- Wright, E. L. 2010, *AJ*, 140, 1868
- Zackrisson, E., Bergvall, N., & Leitet, E. 2008, *ApJL*, 676, 9
- Zhang, W., Kong, X., Li, C., Zhou, H.-Y., Cheng, F.-Z. 2007, *ApJ*, 655, 851

Table 1. Local HAEs

SDSS ID	R.A.	Decl.	redshift	H α EW	$f(H\alpha)$	$\log I_{FUV}$	$\log SFR$	$\log M_*$	12+ $\log[O/H]$	$D_n(400)$
587727179525783616	5.915092	-9.813522	0.053035	667.5	4001.6	8.447	0.481	8.608	8.149	0.898
588015507661455435	6.104308	-1.066375	0.039368	611.7	1085.2	8.784	-0.610	...	8.007	0.912
588015507661979813	7.409042	-1.204444	0.164415	752.8	865.7	9.116	0.675	...	8.155	0.839
588015508199506053	8.835831	-0.746512	0.249825	503.4	773.8	8.819	0.920	...	8.255	0.919
587740588411519244	9.582756	25.219419	0.311599	657.4	597.0	8.841	1.073	9.278	8.412	0.969
587724199349387411	10.226349	15.569384	0.283232	636.7	478.4	8.939	0.873	9.240	...	0.882
587724234248552589	10.653869	16.034079	0.247397	844.6	995.4	11.839	1.668	9.346	8.809	0.855
587731186746196208	12.307815	0.400554	0.159282	896.6	580.6	9.116	0.256	8.942	7.673	0.766
587731514215366775	16.450899	1.080542	0.329321	574.2	273.3	7.890	0.851	...	8.751	1.255
587727180069142712	21.047823	-9.002034	0.229820	913.6	489.1	11.317	0.942	9.071	7.876	0.950
587724232106508428	23.469007	13.702609	0.008670	1330.2	3342.0	...	-1.394	6.598	7.672	0.000
588015507669188698	23.856556	-1.230119	0.177349	564.5	1235.2	8.980	1.068	9.289	8.489	1.028
588015508206190774	24.127474	-0.632222	0.059468	505.1	972.5	8.868	-0.407	...	8.127	0.976
587724232644820997	26.779322	13.941470	0.056623	684.3	3158.3	8.780	0.548	8.420	8.673	0.863
587731512610127975	28.668512	-0.112153	0.018708	664.7	823.0	8.657	-1.221	...	8.775	0.000
587731512610455795	29.539122	-0.110334	0.012072	817.4	2152.9	8.856	-1.412	...	7.933	0.000
587727779743596668	34.720455	-9.205221	0.012708	686.3	2136.4	8.276	-0.962	7.042	8.015	0.000
587727178464624784	35.156929	-9.485357	0.113164	597.2	1955.8	9.439	0.525	9.272	9.270	0.895
587731514224279696	36.810349	1.093360	0.348540	1293.5	856.1	9.226	1.667	...	8.836	1.001
587727177929588906	39.490982	-9.525620	0.280223	667.9	509.4	11.326	0.906	9.230	...	0.776
587727179003723785	40.217499	-8.474285	0.082176	1795.5	4386.1	9.736	0.816	8.457	7.897	0.683
588015509824208968	40.995934	0.556302	0.059319	708.7	1001.1	...	-0.432	...	8.038	0.836
587731514226442382	41.761272	1.258160	0.128720	844.0	1875.2	9.219	1.063	9.034	8.633	0.838
587727180078907412	43.444599	-7.395548	0.004494	789.9	3784.6	9.951	-2.010	6.062	7.953	0.000
587731511543726169	45.454273	-0.882610	0.007318	758.9	1641.3	8.225	-1.998	...	7.677	0.000
587727179006148758	45.839211	-7.989777	0.164813	589.8	1817.3	9.327	0.838	9.121	7.817	0.842
587731514228474146	46.413918	1.189721	0.167591	859.9	453.8	8.129	0.281	...	8.045	0.959
588015509290483920	48.250191	0.103361	0.029164	577.7	1161.1	9.365	-1.023	...	7.895	0.849
587744294975242477	48.357658	5.751317	0.195068	1259.5	993.4	8.972	1.493	9.035	8.151	0.995
587731512082170019	49.026310	-0.438349	0.022894	563.0	1971.2	11.054	-1.208	6.650	8.048	0.846
588015509290877040	49.099861	0.153407	0.202564	854.8	1144.3	9.785	0.882	9.236	...	0.771
587724241767825591	51.556793	-6.586821	0.162033	638.1	1742.2	9.699	1.417	9.206	8.749	0.859
588015510365929716	52.101753	0.909903	0.276351	831.5	816.3	8.693	1.467	...	8.692	0.924
587731513157746887	53.330040	0.292035	0.193820	623.2	1025.7	9.241	0.937	...	8.364	0.932
587731514232275127	55.082912	1.058530	0.321582	530.0	314.4	11.201	0.889	...	8.710	1.182
587731511549427842	58.572277	-0.913758	0.025706	602.7	2305.9	9.212	-0.580	...	7.895	1.130
587727179550294225	62.406769	-5.301616	0.074775	599.3	1696.9	9.217	0.212	8.472	8.041	0.877
758882136838308201	88.771126	83.197517	0.057179	514.5	1076.3	...	-0.446	7.393	8.579	0.939
587725774528643229	113.236320	37.080456	0.139556	524.9	2160.2	9.060	1.242	9.764	8.687	0.917
587732054308094381	115.144371	24.693533	0.192887	564.0	1626.4	...	1.122	9.385	8.387	0.949
587732152555864324	116.991676	23.609142	0.155223	548.9	894.7	...	0.480	9.239	8.125	0.899
588016841241395565	117.026268	19.529713	0.062913	765.3	3074.9	9.269	0.469	8.640	8.620	0.947
587731887343141089	117.146057	31.510386	0.027381	642.6	4367.5	8.270	-0.047	8.030	8.145	0.920
587731681185038501	118.126228	30.268797	0.104871	528.0	1131.6	9.115	0.471	9.145	8.011	0.948
588297865245360528	119.660004	25.432913	0.161057	533.9	2565.8	...	1.370	9.519	8.789	1.031
588007005769892050	120.446251	43.883945	0.084337	530.2	1589.3	9.124	0.337	8.968	8.573	0.965

Table 1—Continued

SDSS ID	R.A.	Decl.	redshift	H α EW	$f(H\alpha)$	$\log I_{FUV}$	$\log \text{SFR}$	$\log M_*$	12+ $\log[\text{O}/\text{H}]$	$D_n(400)$
587731885734625538	121.991661	34.244244	0.022444	1279.5	1851.5	8.252	-0.946	6.787	7.905	0.750
587738947196944678	123.966682	21.939903	0.140995	852.4	1124.3	9.202	0.611	9.047	7.957	0.788
587732577221083492	125.895187	3.221021	0.009771	1355.1	16856.7	10.612	-0.518	6.810	8.128	0.000
587735241709322314	125.979027	28.106043	0.047222	505.5	12206.2	10.336	1.474	8.608	8.833	0.927
587725980151513279	126.377838	50.801239	0.096858	556.0	2543.5	9.488	0.623	8.864	8.477	0.879
587741421636092149	126.418541	18.771444	0.037959	1283.9	2072.9	9.051	-0.218	7.345	7.820	0.843
587731679041290347	126.481354	35.542213	0.002496	1441.0	6282.5	8.842	-1.995	6.040	7.670	0.000
587739114701652062	127.664062	22.250998	0.016886	538.6	5476.6	8.798	-0.304	7.951	8.425	0.936
588010137337200805	128.666870	48.094685	0.342574	890.6	929.5	9.218	2.055	...	8.782	0.860
587731680116867174	129.681839	38.897362	0.147461	620.0	4561.8	9.638	1.353	9.573	8.545	0.936
587741489819025453	130.001556	18.091948	0.072188	824.2	2345.0	9.939	0.777	8.244	8.700	0.807
587742010046808228	130.142105	13.747596	0.226933	769.8	948.2	9.105	1.551	9.275	8.799	0.895
587745403070710009	130.652435	10.553878	0.010318	605.1	2504.7	8.219	-1.191	7.010	7.847	0.000
588010358527951007	131.059311	2.439195	0.091093	560.0	4591.0	...	1.594	9.201	8.830	0.967
587725471207260238	131.365067	53.148048	0.031071	631.5	5260.2	8.594	0.001	8.135	8.312	0.863
587745539973382205	132.484436	10.719072	0.014143	506.8	7399.6	8.527	-0.461	7.668	8.038	0.000
587737809037558040	132.815216	58.681950	0.091864	1384.0	3337.6	9.046	0.817	8.647	7.896	0.720
587745243620638850	133.090485	12.281044	0.075924	812.3	9556.6	9.418	0.983	8.986	8.418	0.812
587741532770074773	133.350372	19.506294	0.236503	564.4	629.5	...	0.819	9.173	8.176	0.887
587726031692103963	135.277344	0.905037	0.110702	507.4	1617.7	9.512	0.625	9.176	8.285	0.950
587741421103611996	136.278595	22.642759	0.125548	500.3	1916.9	9.417	0.700	9.097	8.289	0.895
587731681193754681	136.367004	44.182873	0.065364	568.5	3355.1	9.069	0.546	8.702	8.526	0.895
588010359604052117	136.379486	3.591771	0.039088	591.5	2267.1	8.865	-0.064	8.061	7.890	0.862
587732048406249534	136.618698	44.981819	0.074672	566.1	2915.6	8.884	0.888	8.777	8.691	0.941
587734622171889671	138.037277	36.373997	0.165166	559.4	1500.0	9.169	1.119	9.231	8.828	0.894
587732049481039908	138.645645	47.035343	0.027269	569.9	8656.9	9.150	0.157	8.269	8.016	0.882
587741817314738195	139.170761	18.468864	0.021771	534.0	2973.1	9.026	-0.595	7.438	8.040	0.885
587745243087372534	141.384872	14.053627	0.301211	533.1	659.8	9.364	1.192	9.164	8.267	0.896
588013384341913605	141.501694	44.460049	0.180667	578.0	1770.6	9.861	1.063	9.129	8.482	0.884
587742014876745993	141.869492	17.671837	0.288328	509.3	578.0	9.063	1.032	9.225	8.307	0.910
587734622173462551	142.026337	38.132477	0.060717	739.6	5650.9	8.841	0.723	8.723	8.541	0.853
587725075530317872	142.326645	0.470347	0.093874	888.4	1866.7	9.511	0.444	8.560	8.001	0.798
587725817478840384	142.526810	60.448166	0.013659	587.4	8243.8	9.591	-0.750	7.320	8.062	0.000
587739114708402325	142.907227	29.333946	0.330326	641.7	720.0	9.944	1.885	...	8.848	1.068
588010136268505157	143.509933	55.239777	0.002565	894.8	5601.8	9.437	-1.149	6.041	7.670	0.000
587734621637247125	143.911865	38.631794	0.137483	650.1	1823.5	8.848	1.082	9.260	8.656	0.871
587735343188934969	144.097046	9.000285	0.223567	672.6	923.0	8.907	1.590	9.237	8.741	0.882
587741392646504460	144.213989	26.717690	0.294546	510.1	933.1	9.652	1.246	9.385	8.468	0.904
588017979952922757	145.726135	34.069969	0.022487	795.7	1233.7	8.691	-1.102	6.833	7.836	0.848
587725073921278043	146.007797	-0.642272	0.004810	1534.4	21890.4	8.757	-1.049	6.690	7.867	0.000
587734623786238071	146.826477	41.637905	0.004658	870.0	3060.5	7.680	-1.791	6.435	7.909	0.000
588848900972216400	147.597183	0.708133	0.097702	552.3	3004.3	10.388	1.087	8.785	8.787	0.846
587728930273493055	147.882355	52.993347	0.046263	951.8	5236.0	...	0.288	8.195	7.990	0.820
587727944033108132	148.112335	2.299958	0.119123	511.9	3007.5	...	1.274	9.307	8.768	0.935
587732152033345685	149.076309	43.124393	0.275709	538.1	982.0	13.432	1.674	9.280	8.826	0.943
587742062133117119	151.835388	19.563786	0.031410	579.3	1430.3	8.933	-0.657	7.454	7.949	0.869

Table 1—Continued

SDSS ID	R.A.	Decl.	redshift	H α EW	$f(H\alpha)$	$\log I_{FUV}$	$\log \text{SFR}$	$\log M_*$	12+ $\log[\text{O}/\text{H}]$	$D_n(400)$
587728309631975445	151.943817	2.874571	0.023492	580.8	4678.0	9.180	-0.347	7.596	8.123	0.907
587741817320505351	152.636688	22.011009	0.004226	1038.6	9742.0	9.281	-1.563	6.525	7.928	0.000
587735348561444896	152.677261	12.921337	0.061313	574.1	7544.8	...	0.733	8.679	8.548	0.857
587745541055971461	152.747086	15.706535	0.055632	802.3	5601.7	9.488	0.479	8.393	7.958	0.832
587738410863493299	152.987869	13.139479	0.143776	1395.2	2139.5	...	0.808	9.241	7.988	0.689
587738409789751347	153.112595	12.343749	0.009565	807.2	8293.9	...	-0.814	7.236	8.095	0.000
587742061597032613	153.744339	19.538765	0.012629	615.4	1542.3	...	-1.409	6.536	7.852	0.000
587739376706387983	153.859955	30.914406	0.091751	537.9	2986.5	9.991	1.065	9.017	8.812	0.952
587735661550698508	154.102158	37.912769	0.003879	597.0	10978.4	9.210	-1.462	6.582	7.675	0.000
587734861609566213	154.124542	7.568038	0.182909	575.6	1859.0	9.148	1.554	9.443	8.695	0.924
588017605211390138	154.513519	41.105858	0.237018	679.0	721.2	9.306	1.142	9.173	8.644	0.794
587733081878888643	154.731064	51.924393	0.129398	520.0	2320.1	8.893	1.003	9.342	8.154	0.964
587728881414897699	156.121887	5.414172	0.033191	525.6	6362.6	9.174	0.046	8.191	7.902	0.881
587732578845786234	157.912231	7.265705	0.252536	568.7	446.5	...	0.675	8.946	8.215	0.929
587741490367889543	158.112335	27.298689	0.192490	626.1	1302.3	9.891	1.233	9.286	8.697	0.913
587732134842531847	160.176544	49.206581	0.005011	1454.6	7045.5	7.843	-1.505	6.329	8.030	0.000
587742014884544559	160.289993	21.361889	0.003976	599.2	13890.7	9.532	-1.273	6.766	7.962	0.000
588017979421622307	160.668793	37.917389	0.166793	612.9	2133.4	...	1.521	9.373	8.751	0.913
587728879269642285	161.240799	3.886987	0.012873	1464.5	10315.3	10.044	-0.846	6.796	7.870	0.000
58773486322324735	161.335083	9.396972	0.054873	600.2	6184.5	8.380	0.897	8.873	8.544	0.985
588848901515182119	161.478241	1.068288	0.026199	890.7	11053.6	9.170	0.119	8.056	8.547	0.790
587738410330357781	161.724945	13.779382	0.010610	916.4	4409.3	8.882	-1.153	6.806	8.042	0.000
587742863668412459	162.635483	15.635085	0.084427	1045.3	5962.5	9.416	0.894	8.649	8.062	0.800
587739096444698642	162.670166	34.496483	0.052196	560.4	3332.6	9.077	0.245	8.324	8.050	0.910
588017705070886933	163.321625	12.777442	0.021807	523.3	4132.4	8.103	-0.219	8.070	8.072	0.887
587742062138621980	164.967575	21.708441	0.115118	607.4	4306.8	8.260	1.183	9.716	8.590	0.938
588848900980015266	165.318329	0.804029	0.212857	1190.1	1025.2	10.368	1.059	9.144	8.000	0.803
587741600950845470	165.891815	25.404541	0.155750	600.4	3250.1	8.744	1.463	9.592	8.575	0.924
587741490907971706	166.243927	29.137699	0.002139	686.8	11346.6	10.537	-2.520	6.109	7.994	0.000
587742015424233589	167.160431	22.636049	0.023815	630.1	4309.1	9.115	-0.461	7.416	8.090	0.882
588017606290178168	169.363617	45.012020	0.184647	1267.6	859.8	7.988	0.821	9.276	8.144	0.780
587742775628005405	169.442932	17.740192	0.004916	538.2	6140.8	9.452	-1.437	6.621	8.019	0.000
587726033317789755	169.686325	2.908351	0.020327	1284.1	4852.2	10.192	-0.636	7.577	8.059	0.705
587739607548362788	170.779007	30.478922	0.005361	602.8	10808.8	10.285	-1.248	6.154	8.689	0.000
588009370688553009	172.130554	61.215439	0.084348	928.3	2451.9	9.144	0.849	8.680	8.649	0.876
587735696440885344	172.818207	57.066330	0.005561	609.6	1984.4	7.771	-1.694	6.507	7.897	0.000
587732484357161015	173.690506	50.100925	0.026005	623.1	10756.5	9.864	0.013	8.047	8.421	0.864
588017111292969009	174.099274	47.158077	0.010177	911.2	5198.8	9.470	-1.221	6.675	7.934	0.000
587739408388980778	174.342255	35.407413	0.194313	562.8	2162.4	10.357	1.611	9.331	8.740	0.927
587742981247795242	175.087631	60.327374	0.146754	539.9	2470.4	9.891	0.873	...	8.653	0.845
587739647821807686	175.281204	32.427006	0.006015	601.2	9006.3	10.478	-1.797	6.041	7.922	0.000
587739609697878126	175.951233	32.716095	0.073985	915.4	3054.6	9.168	0.147	8.550	...	0.860
588010879831113781	175.998093	5.365164	0.099142	596.1	1768.2	8.817	0.792	8.784	8.709	0.853
587748930312994906	176.705582	0.896104	0.056519	540.0	849.5	8.865	-0.407	7.744	7.976	0.813
587742191512715306	177.113907	25.769936	0.045117	854.5	9305.0	9.024	0.550	8.507	8.061	0.836
587742775094345789	177.170303	17.942505	0.079110	919.6	4043.8	9.551	0.719	8.605	8.257	0.784

Table 1—Continued

SDSS ID	R.A.	Decl.	redshift	H α EW	$f(H\alpha)$	$\log I_{FUV}$	$\log \text{SFR}$	$\log M_*$	12+ $\log[\text{O}/\text{H}]$	$D_n(400)$
587739304214265947	177.268524	35.039696	0.021131	520.5	5706.4	8.944	0.064	7.707	8.670	1.022
587735348571996236	177.511383	15.023189	0.002448	834.3	22601.2	...	-1.536	6.583	8.069	0.000
587748928166101081	178.197968	-0.668794	0.004619	590.0	3819.9	8.692	-1.784	6.363	7.966	0.000
587739096987271268	178.512695	36.850090	0.268020	743.3	670.5	8.568	0.707	9.055	...	0.789
587731891114803229	178.868073	57.664436	0.017262	1023.5	15064.6	9.550	-0.176	7.660	7.914	0.780
587735346962497616	180.139252	13.718885	0.066750	1110.9	6000.8	9.444	0.066	8.471	...	0.838
587726033859248332	180.231827	3.401094	0.084712	777.2	2024.7	...	0.417	8.482	7.907	0.834
587726032248701055	180.342972	2.185653	0.003251	1014.1	3213.4	7.723	-1.996	6.086	7.670	0.000
587741709958840329	180.457916	28.102964	0.055879	672.2	2718.8	9.224	0.169	8.241	8.039	0.838
587739408391471112	181.289520	35.830231	0.119502	746.0	2759.7	9.884	1.394	9.065	8.770	0.816
587741531715797096	181.343231	28.946814	0.107620	1303.6	1982.1	9.408	0.714	8.832	7.900	0.761
588011122502336742	181.772125	61.586613	0.262101	2270.8	448.2	12.980	0.723	9.048	8.181	0.839
587741491451002960	182.393707	30.890612	0.219277	574.2	1534.2	10.206	1.501	9.259	8.718	0.862
588017626154598555	182.534775	44.651821	0.022742	675.4	1456.2	8.300	-0.899	7.243	8.028	0.934
588017567099388030	182.658813	13.023331	0.008039	873.0	2874.4	7.886	-1.351	6.625	7.999	0.000
587742061609156755	183.351196	22.542812	0.162278	623.6	440.0	8.549	0.246	8.658	8.060	0.846
587733079202070556	183.510345	53.754841	0.003055	853.4	4177.1	8.413	-1.939	6.025	7.707	0.000
587735696443506837	184.006226	57.577858	0.286866	1084.4	1180.1	...	1.242	9.038	...	0.878
587735349111947338	184.766602	15.435700	0.195579	1094.5	1714.8	9.846	1.129	9.266	7.893	0.763
587742012747022361	184.884247	21.556944	0.140986	645.4	3180.9	10.048	1.615	9.185	8.811	0.873
588298662500171878	185.610733	47.066746	0.186958	611.5	2524.3	9.532	1.762	9.568	8.796	0.934
587742954397630497	185.818893	4.836145	0.017845	520.5	5224.2	8.804	-0.811	...	8.062	0.864
587739097526829082	186.152985	37.410152	0.040380	548.8	3170.1	9.265	-0.095	7.864	7.907	0.897
588010878225088680	186.549576	4.260018	0.094233	984.5	2221.1	8.544	0.579	...	8.262	0.737
588017729763016856	187.033600	7.912061	0.068031	582.2	2076.4	8.842	0.062	...	8.250	0.912
588017702933758072	187.702515	12.045229	0.004185	577.7	5388.9	8.474	-1.689	6.563	7.861	0.000
588848899379822768	189.216797	-0.589419	0.008531	905.2	1317.8	9.443	-1.916	6.129	8.045	0.000
588017728690257952	189.259445	6.925279	0.005381	1556.0	20058.4	10.698	-0.819	...	8.707	0.000
587735696981688461	189.505127	58.020718	0.083989	917.5	1786.0	8.612	0.443	8.464	8.403	0.819
588017109686943854	189.515656	46.305592	0.098789	740.7	2442.8	8.442	1.142	9.046	8.590	0.957
587732771595419747	189.528702	10.165563	0.003795	1106.1	6387.0	7.860	-1.715	6.467	7.974	0.000
587725039022768267	190.497253	-3.667338	0.009240	611.5	2370.1	8.569	-1.425	6.590	7.896	0.000
588017977284427855	190.820267	38.769154	0.023091	531.9	2965.5	8.827	-0.497	7.670	8.083	0.967
587726032253419628	191.097427	2.261253	0.239378	777.5	2103.5	9.553	1.631	9.570	8.688	0.840
588017979968847957	191.170593	40.708172	0.017520	967.9	2442.9	8.697	-0.817	7.097	8.076	0.838
588017992294662200	191.287720	10.727820	0.165673	719.0	3626.7	9.292	1.616	9.564	8.770	0.874
587738570853974145	192.061798	15.974835	0.278174	622.2	768.9	8.756	1.311	9.323	8.644	0.990
588017570848768137	192.144318	12.567482	0.263408	669.4	881.5	10.583	1.002	9.127	8.255	0.901
587732483288989834	193.416092	49.516125	0.231133	513.5	426.3	9.095	0.589	8.964	8.133	0.940
587724649799942319	193.858643	-2.226135	0.051885	1278.5	1582.4	9.196	-0.327	7.667	...	0.768
587726014538383550	194.380783	1.933281	0.252218	577.6	560.5	11.321	1.238	9.232	8.598	1.016
587738950417448968	195.763855	35.857948	0.060287	571.7	4688.5	...	0.573	8.741	8.526	0.905
587739098067107878	195.976852	37.233856	0.035953	518.6	5864.9	9.103	0.186	8.335	8.562	0.879
587739304758083615	196.600800	35.228622	0.016196	650.3	5764.7	...	-0.438	7.516	8.017	0.845
587742062151467120	196.734818	22.694004	0.274104	521.6	451.1	8.173	0.887	9.228	8.326	0.916
587733080816091172	196.869583	54.447128	0.032524	544.9	8271.5	10.657	0.005	7.781	8.568	0.918

Table 1—Continued

SDSS ID	R.A.	Decl.	redshift	H α EW	$f(H\alpha)$	$\log I_{FUV}$	$\log \text{SFR}$	$\log M_*$	$12+\log[\text{O}/\text{H}]$	$D_n(400)$
588848899383623800	197.812668	-0.466085	0.230964	575.0	801.3	8.759	1.420	9.357	8.693	0.948
587741724973924354	199.480362	23.261173	0.024026	582.0	2775.0	8.332	-0.357	7.912	8.086	0.914
587724648191885354	199.604355	-3.418798	0.128790	617.3	2723.1	9.483	1.544	9.445	8.930	0.996
587733080280203402	200.460190	53.691071	0.032849	620.9	1215.2	...	-0.483	7.600	8.103	0.845
587729775021981805	200.947754	-1.547763	0.022464	1460.7	4136.0	9.764	-0.727	7.042	7.870	0.723
587742062153236558	201.152542	22.183628	0.075391	747.1	2376.6	9.070	0.446	8.421	8.485	0.879
587729385546186821	201.229340	57.752960	0.116320	528.5	1764.5	8.590	0.928	9.268	8.754	0.917
587735429081530430	201.332870	48.040596	0.016369	669.9	3471.1	8.694	-0.717	7.423	8.024	0.867
587739406251327528	201.455933	33.065105	0.014620	534.3	9028.6	9.043	-0.458	7.720	8.359	0.927
587726031184330774	201.727585	1.229622	0.179626	679.3	2060.7	9.441	1.060	9.296	8.075	0.928
588017947210154051	201.847031	40.367821	0.010498	688.7	1261.1	8.706	-1.700	6.273	7.802	0.000
588017605226594329	202.183563	43.930698	0.027969	559.8	14970.0	9.654	0.333	8.336	8.610	0.882
587742773494218867	202.220657	15.992878	0.022747	866.1	3471.1	9.281	-0.680	7.179	7.845	0.838
587742903405379689	202.318985	17.005835	0.094252	738.3	4768.0	10.383	1.328	8.970	8.811	0.863
587742774031220880	202.470200	16.342064	0.180808	778.9	1996.8	9.298	1.118	9.398	8.361	0.845
588017948284092523	202.536865	41.123695	0.027297	539.9	971.7	8.266	-0.675	7.280	8.005	0.949
588017949357834271	202.862137	41.863415	0.011701	744.3	5782.7	8.741	-0.885	7.159	7.854	0.000
587733411516842159	203.692856	53.824303	0.167942	502.2	888.1	8.726	1.007	9.018	8.781	0.933
587742550137241839	203.757736	18.527227	0.314059	679.4	465.2	9.626	0.940	9.044	...	0.951
588017726556143757	203.906677	8.030304	0.123465	847.5	1983.8	9.466	0.755	8.982	7.996	0.834
587738953104556058	203.950333	37.029358	0.056500	586.5	2891.1	...	0.482	8.441	8.553	0.954
587738570859413642	204.867935	15.278371	0.192017	932.6	1808.1	9.872	1.609	9.298	8.676	0.787
587739608635146287	205.485336	30.519339	0.003196	533.2	10491.2	8.374	-1.504	6.979	8.107	0.000
587735666377883763	206.114014	56.024929	0.070633	687.8	6400.2	8.839	1.033	9.146	8.549	0.912
587739609709346918	206.848175	31.215101	0.119167	569.9	1492.4	8.979	0.552	9.374	8.269	0.913
587739811557867563	207.029114	26.405453	0.057039	555.6	4357.2	8.697	0.576	8.807	8.147	0.911
587742062693187673	208.642700	21.831629	0.110722	615.3	1465.5	...	0.663	9.765	8.289	0.929
588848901536481289	210.078918	1.081637	0.121090	865.0	2392.8	...	0.921	8.991	8.564	0.862
587735695913386093	211.119293	54.397999	0.000970	1126.5	17817.4	...	-1.935	6.036	8.742	0.000
587726102556377282	211.855453	5.477178	0.084972	579.5	1425.3	9.111	0.166	8.444	8.002	0.890
587735696987389965	212.486496	54.946915	0.077313	721.9	6030.7	9.581	1.364	8.988	8.787	0.883
588298661971820653	212.746735	43.046371	0.065605	613.0	4279.9	10.072	1.277	8.449	8.752	0.909
587742551751721066	213.140366	18.500360	0.007383	568.7	3461.5	...	-1.410	6.882	7.994	0.000
587735696987717870	213.630035	54.515598	0.227058	508.9	393.8	9.521	0.515	9.033	8.201	0.870
587739380986216524	214.643311	31.211664	0.163290	531.8	433.5	9.977	0.310	8.572	7.891	0.910
587739843771695144	214.713028	21.044373	0.008547	1156.2	6710.1	...	-1.161	6.632	7.674	0.000
587722982292521071	215.559616	-0.655451	0.105870	572.2	1330.7	9.785	0.268	8.729	8.016	0.811
587739826591563799	215.928650	22.957996	0.032848	743.2	4621.7	9.421	-0.189	7.650	7.805	0.823
588017114517536797	216.023865	42.279533	0.184816	1083.9	2550.9	10.255	1.675	9.284	8.787	0.770
587728920058200166	216.579788	62.463882	0.111854	584.1	1431.6	9.294	0.403	9.078	8.574	0.867
588017948825813029	216.617355	38.382965	0.022302	535.4	2074.6	9.449	-0.805	7.189	7.939	0.889
588017979977826415	217.022964	36.452888	0.086236	530.5	3105.9	8.794	0.574	8.841	8.022	0.870
587736525374357550	217.445862	6.726379	0.173502	850.2	4236.5	10.481	1.985	9.445	8.810	0.817
587726031728345220	218.042328	1.431060	0.136353	619.1	1768.1	9.372	1.142	9.005	8.808	0.905
587742577530372265	219.488220	17.322380	0.201980	1069.5	950.0	9.659	0.766	9.215	...	0.774
587726014549328120	219.517548	1.559333	0.312374	534.2	747.9	10.290	1.790	9.366	8.841	0.944

Table 1—Continued

SDSS ID	R.A.	Decl.	redshift	H α EW	$f(H\alpha)$	$\log I_{FUV}$	$\log SFR$	$\log M_*$	12+ $\log[O/H]$	$D_n(400)$
587736545772044617	220.114777	5.531906	0.005195	976.7	2689.7	8.539	-1.817	6.170	7.789	0.000
587729777446945029	220.630737	-2.164453	0.293644	899.7	830.3	10.028	1.118	9.112	7.999	0.717
587726101486764162	221.172363	4.161592	0.038811	841.9	1110.9	7.717	-0.702	7.359	7.679	0.833
588011218602623163	221.949203	57.083385	0.285271	641.3	499.2	8.609	1.074	8.997	8.865	0.890
587729778521342037	222.022400	-1.182697	0.027412	792.0	14736.6	9.634	0.475	8.090	7.951	0.869
587733398637314061	222.735794	48.623966	0.091899	536.6	4395.6	9.596	0.973	9.170	8.539	0.891
588018055652769997	223.648239	45.482330	0.268552	505.7	786.5	9.707	1.692	9.269	8.927	1.001
588023721783328799	223.690521	20.527960	0.015779	508.9	2959.8	...	-0.984	7.179	7.992	0.000
588017626705166406	223.775284	38.137966	0.027702	703.9	5563.8	9.567	0.060	7.601	8.627	0.817
587739828742389914	224.396408	22.533831	0.148653	923.9	2325.5	9.286	1.009	9.241	8.296	0.780
587736976343171214	224.484177	30.862373	0.076537	539.6	1927.9	8.947	0.704	8.536	8.692	0.943
588011103712706632	226.616592	56.450748	0.278579	502.9	742.5	8.949	1.691	9.445	8.899	1.049
587729227147968579	226.869537	59.986984	0.182027	542.6	1727.1	9.325	1.533	9.436	8.757	0.974
587733397565341781	227.287689	45.719120	0.048121	558.7	4671.8	8.916	0.349	8.359	8.569	0.948
588017627780153375	227.392395	37.529476	0.032549	1348.0	6715.9	8.947	0.329	7.784	7.921	0.792
587733399712628848	228.053574	47.275188	0.053158	564.5	9973.9	8.715	1.012	9.119	8.611	0.938
587739629560332485	228.229614	24.219585	0.073510	539.8	1591.2	9.309	0.114	8.389	8.040	0.880
587733412061577276	229.483307	46.418430	0.019327	594.6	2838.0	8.866	-0.767	7.241	8.003	0.899
588011218605179021	230.190155	53.635342	0.207637	725.7	629.5	9.168	0.683	9.234	8.407	0.944
587739845925732735	230.661835	18.914272	0.182822	875.9	509.3	...	0.619	9.171	7.998	0.889
588017977836240925	230.884140	29.520021	0.068164	780.7	3333.1	9.164	0.344	8.405	7.986	0.822
587736976882663541	230.962494	28.616953	0.085434	620.5	1934.2	9.911	0.473	8.582	8.614	0.893
587732484375314456	232.071594	39.947338	0.064470	633.4	2909.7	8.869	0.449	8.753	8.552	0.831
588848900472373334	232.128006	0.294496	0.113605	505.2	2186.0	9.149	0.448	9.273	7.670	0.957
587736618784587856	232.671951	31.018482	0.087004	516.8	4146.2	...	0.934	9.243	8.300	0.938
587742577536205016	232.982117	14.321038	0.031074	728.8	1892.1	8.156	-0.424	7.549	7.824	0.850
587742061093322861	233.639023	14.913211	0.073269	600.4	4016.0	9.533	0.597	8.758	8.134	0.902
587729229297090692	234.405319	58.794586	0.214291	722.0	668.8	8.643	0.830	9.097	8.485	0.903
587735666387058818	235.333435	45.605324	0.202897	800.5	1571.6	10.129	1.627	9.269	8.757	0.931
587736915148996802	236.431473	8.967041	0.037724	1086.2	13056.6	10.073	0.492	8.041	7.841	0.784
587726101493579972	236.727264	3.150609	0.208937	613.6	2060.5	9.310	1.313	9.545	8.545	0.916
587736542027710819	236.755005	5.807413	0.230501	635.0	719.2	9.296	1.350	9.206	8.779	0.872
587726102030451047	236.787933	3.603900	0.231209	777.0	710.0	8.450	1.242	9.259	8.659	0.951
587739720845230356	237.615784	19.349661	0.212293	551.9	1531.4	9.688	1.874	9.422	8.868	0.848
587739652107600089	238.041687	21.053413	0.233148	555.8	628.5	9.161	0.923	9.193	8.264	0.809
587742061095551365	238.709274	13.435967	0.148752	901.5	1005.4	8.679	0.800	9.127	8.344	0.827
587736975276048497	239.384613	23.347342	0.032834	732.1	13564.8	9.772	0.531	8.049	8.651	0.959
587733399717413034	239.935684	40.556999	0.226811	500.1	682.6	9.522	0.828	9.139	8.269	0.869
587736915687964980	241.152771	8.333086	0.312282	662.1	552.5	9.240	0.942	9.183	8.041	0.906
587729409147666501	241.417877	50.754395	0.012880	600.7	2121.6	9.534	-1.437	6.275	8.084	0.000
587739844320166055	241.614731	13.929967	0.107036	780.1	3672.8	10.099	1.296	8.866	8.711	0.824
588018253759054025	242.043182	35.469250	0.032705	1296.1	1960.0	8.993	-0.382	7.309	7.870	0.760
587739385278890314	243.373352	20.090286	0.051053	546.5	726.2	8.791	-0.481	7.610	7.978	0.922
587736976351822098	244.027786	21.638210	0.288249	529.5	629.6	9.044	0.623	9.099	...	0.893
587742628534354235	244.070374	9.354526	0.048400	562.3	2155.5	8.338	0.077	8.189	8.110	0.980
587739706886062320	245.469055	15.315551	0.034341	672.1	7771.3	8.976	0.711	8.377	8.711	1.147

Table 1—Continued

SDSS ID	R.A.	Decl.	redshift	H α EW	$f(H\alpha)$	$\log I_{FUV}$	$\log \text{SFR}$	$\log M_*$	12+log[O/H]	$D_n(4000)$
587745968930029927	245.681107	16.605579	0.149523	542.6	1911.6	10.843	1.595	...	8.794	1.012
587722982842761249	246.042145	-0.367383	0.031327	649.5	14186.6	9.371	0.483	8.298	8.257	0.899
587739810501361893	246.963211	13.587149	0.016464	540.5	5675.7	9.042	-0.347	7.776	8.577	0.954
587739720849555951	247.051987	15.199133	0.316043	576.9	416.7	8.978	0.900	9.181	...	0.959
588018253224935626	247.114746	30.914915	0.114333	567.3	1605.6	9.261	0.074	9.064	7.670	0.925
587729408620495044	258.152618	32.275951	0.011950	797.3	3946.4	...	-1.065	7.050	7.868	0.000
587725503949177426	260.040924	54.359188	0.293770	790.4	321.1	8.847	0.622	8.875	...	0.866
587725576962244831	261.776398	59.817295	0.347100	502.7	522.0	...	1.663	0.993
587725576426618961	262.277313	56.888676	0.015791	503.9	5343.1	8.911	-0.310	7.715	8.969	1.018
587725577500360837	263.755188	57.052376	0.047232	1347.3	17026.0	9.705	1.155	8.596	8.770	0.799
587727214417871520	315.309967	-5.919530	0.196179	561.8	1578.1	9.207	1.010	9.485	8.368	0.920
587731174918062687	316.967316	1.214631	0.175984	689.2	660.8	8.644	0.467	9.036	8.013	0.868
587726877265559558	318.862823	-7.997601	0.028449	629.7	4729.1	9.666	-0.199	7.616	8.082	0.907
587730774410068219	323.657532	11.419499	0.022039	578.3	5204.3	10.794	-0.998	6.831	8.429	0.926
587731187802767922	333.112244	1.143138	0.210114	561.5	465.3	8.104	0.617	0.956
587734304877707550	333.179413	0.113483	0.177042	615.3	696.9	9.671	0.612	...	8.572	0.959
587734304878035106	333.846069	0.046320	0.077447	769.5	2854.2	9.130	1.015	...	8.711	0.843
587731186193530964	336.292206	-0.198011	0.066681	724.3	4011.3	9.590	0.437	8.401	7.979	0.825
587727222478667784	339.629669	14.008272	0.020607	955.9	3569.8	9.742	-0.769	6.721	7.713	0.802
587731187271336095	345.541687	0.827455	0.033118	853.6	2106.8	8.976	-0.558	...	7.727	0.825
587731187810042042	349.763550	1.148190	0.030129	575.0	1857.7	8.859	-0.469	...	7.953	0.991
587731186201460957	354.466370	-0.166820	0.071730	727.8	1832.8	9.203	0.296	...	8.019	0.844
588015510341943481	357.280731	0.932718	0.185753	511.3	441.1	9.487	0.215	...	8.152	0.990

Note. — Col.(1): SDSS object ID. Col.(2): Right Ascension (J2000). Col.(3): Declination (J2000). Col.(4): Redshift. Col.(5) H α equivalent width of \AA , from MPA-JHU value added catalog for SDSS DR7. Col.(6): H α line flux in units of $10^{-17} \text{ erg s}^{-1} \text{ cm}^{-2}$, from MPA-JHU value added catalog for SDSS DR7. Col.(7): FUV luminosity surface density in units of $L_\odot \text{ kpc}^{-2}$. FUV luminosity is derived using GALEX FUV magnitude, and is divided by r_{hl}^2 while r_{hl} is half-light radius in SDSS u -band. Col.(8): log of the star formation rate in units of $M_\odot \text{ yr}^{-1}$, from MPA-JHU value added catalog for SDSS DR7. Col.(9): log stellar mass in units of M_\odot from MPA-JHU value added catalog for SDSS DR7. Col.(10): 12+log[O/H] from MPA-JHU value added catalog for SDSS DR7. Col.(11): $D_n(4000)$ from MPA-JHU value added catalog for SDSS DR7. Col.(12): Comment for each object. We marked objects that are identified as Wolf-Rayet galaxies (Brinchmann et al. 2008) as ‘WR’.

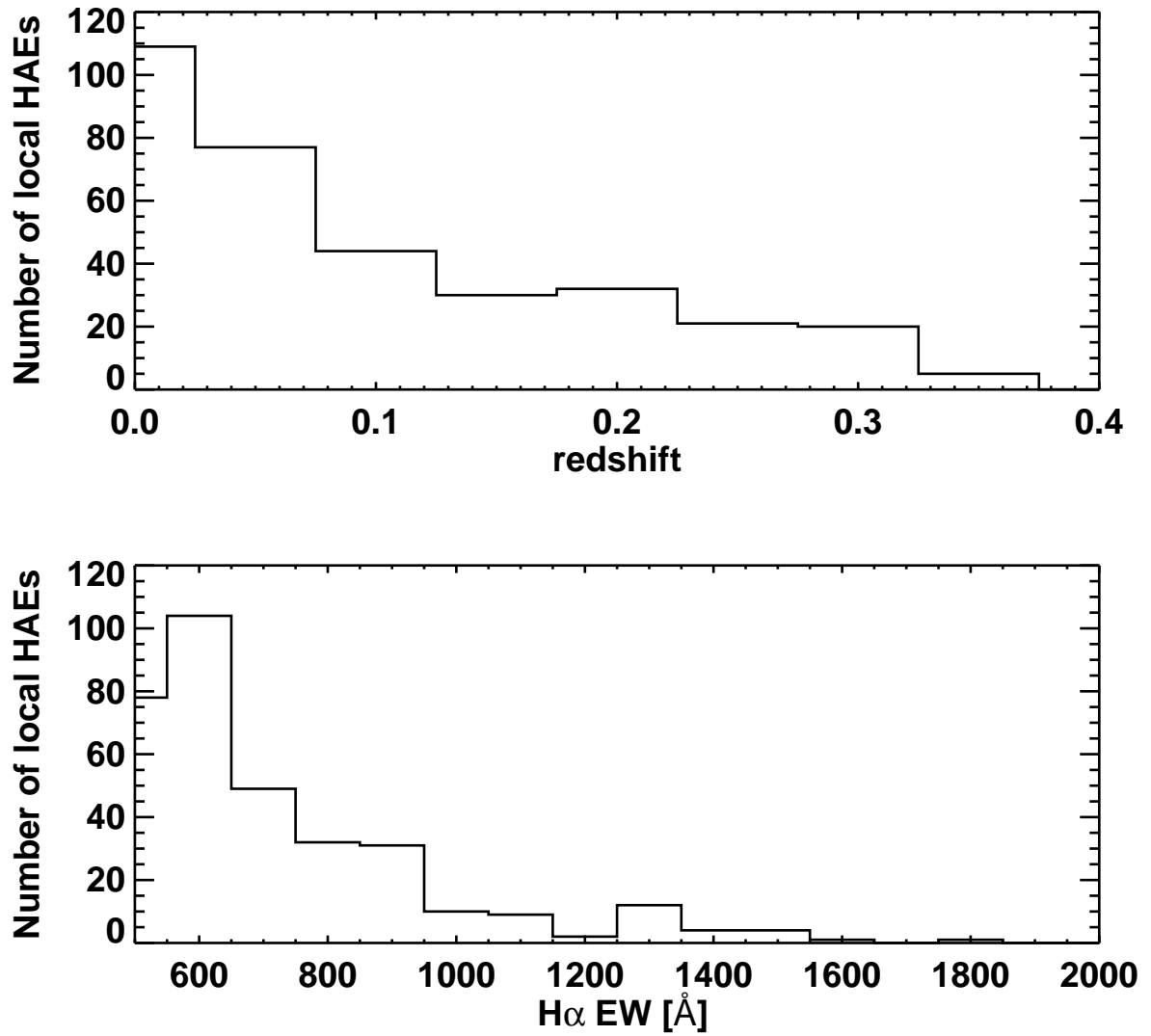


Fig. 1.— H α EW distribution (top) and redshift distribution (bottom) of 299 local HAEs. The EWs are the values in the observed frame, not in the rest frame.

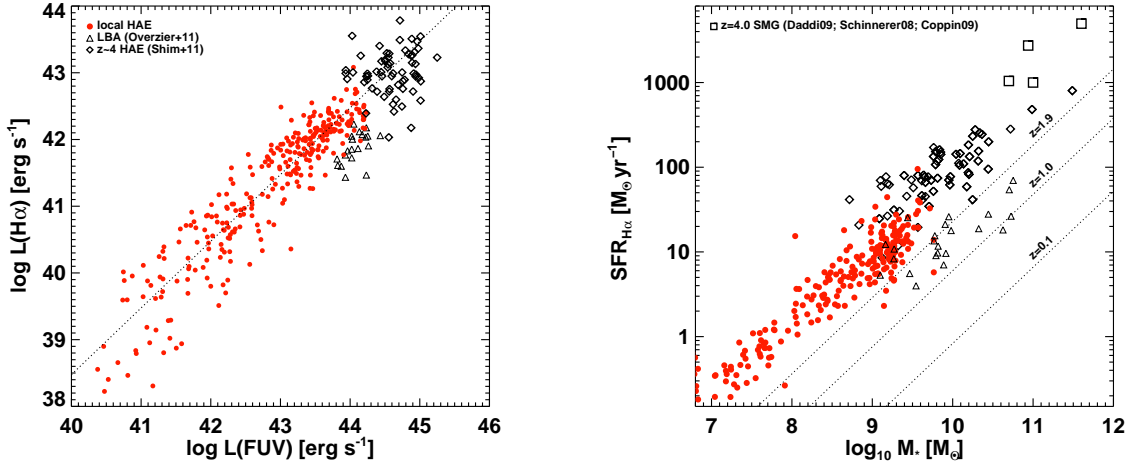


Fig. 2.— (*Left*): Comparison between H α and FUV luminosity (λL_{λ} at 1500 Å) of local HAEs (filled circles), local Lyman break analogs (triangles; Overzier et al. 2011) and $z \sim 4$ HAEs (Shim et al. 2011; diamonds). The H α and UV luminosity of local HAEs is lower than that of $z \sim 4$ HAEs by more than an order of magnitude, yet the H α /UV luminosity ratio is consistent for both galaxy populations. The dotted line is a linear fit to describe $L(\text{H}\alpha)$ vs. $L(\text{FUV})$ of local HAEs, and its slope value is almost unity (0.99). $z \sim 4$ HAEs lie along this line, implying that $z \sim 4$ HAEs are scaled-up versions of local HAEs. LBAs lie below the dotted line, suggesting that their H α luminosity is on average by a factor of 3 lower than HAEs with the same UV luminosity (*Right*): Comparison of SFR per unit stellar mass for local HAEs, LBAs and $z \sim 4$ HAEs. The SFR is derived from the aperture-corrected (see Section 2.1) H α luminosity, using the relationship in Kennicutt (1998). As the overplotted dotted lines indicate, star-forming galaxies appear to form a tight correlation. The SFR per unit stellar mass increases as the redshift increases (Elbaz et al. 2007; Noeske et al. 2007; Daddi et al. 2007). $z \sim 4$ HAEs produce SFR per unit stellar mass comparable to $z = 2.8 - 4.0$ submillimeter galaxies (Daddi et al. 2009; Schinnerer et al. 2008; Coppin et al. 2009). Local HAEs show consistent SFR per unit stellar mass as $z \sim 4$ HAEs while LBAs lie well below the correlation, suggesting that local HAEs are more robust analogs of $z \sim 4$ star-forming galaxies with comparably high star formation efficiency. The high mass end of the stellar mass distribution of local HAEs overlaps with the low mass end for $z \sim 4$ HAEs at $10^9 - 10^{10} M_{\odot}$. There are however observational selection effects against identifying lower mass high-redshift HAEs.

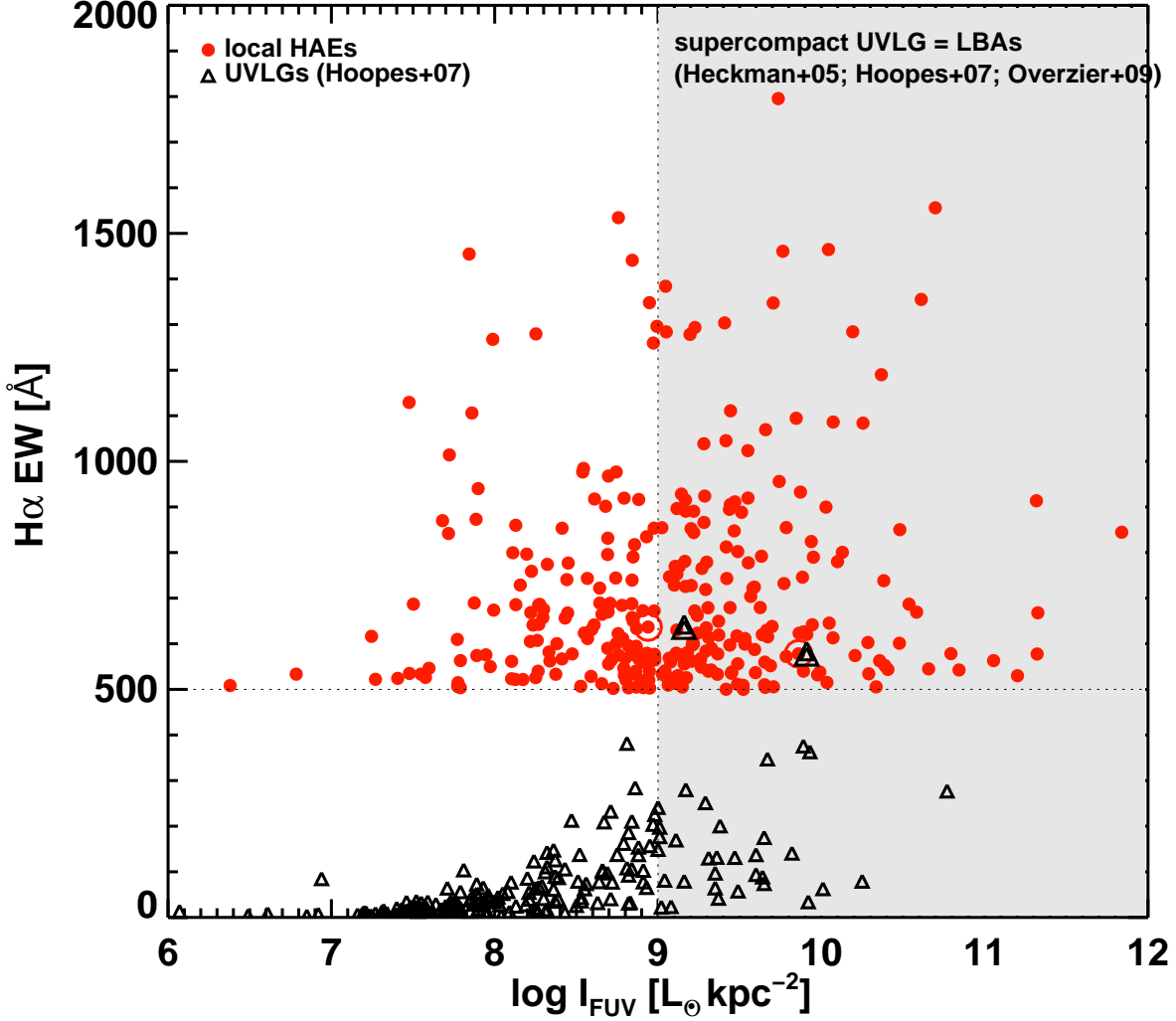


Fig. 3.— Comparison between the UV surface luminosity and $H\alpha$ EW of local HAEs and LBAs. LBAs are a subset of UV-luminous galaxies (UVLGs, $L_{FUV} > 10^{10.3} L_{\odot}$; Heckman et al. 2005; Hoopes et al. 2007) that have relatively high UV surface luminosity ($I_{FUV} > 10^9 L_{\odot} \text{ kpc}^{-2}$). In this plot, local HAEs are plotted as filled circles, and UVLGs (Hoopes et al. 2007) are plotted as open triangles. Shaded region indicates the region where supercompact UVLGs, i.e., LBAs, fall. Although the total UV luminosity is not as luminous as that of LBAs, nearly 50% of the local HAEs have as high a UV surface luminosity as that of LBAs. Only two objects (symbols enclosed with larger symbols) are found to be overlapping between the local HAE and UVLG sample.

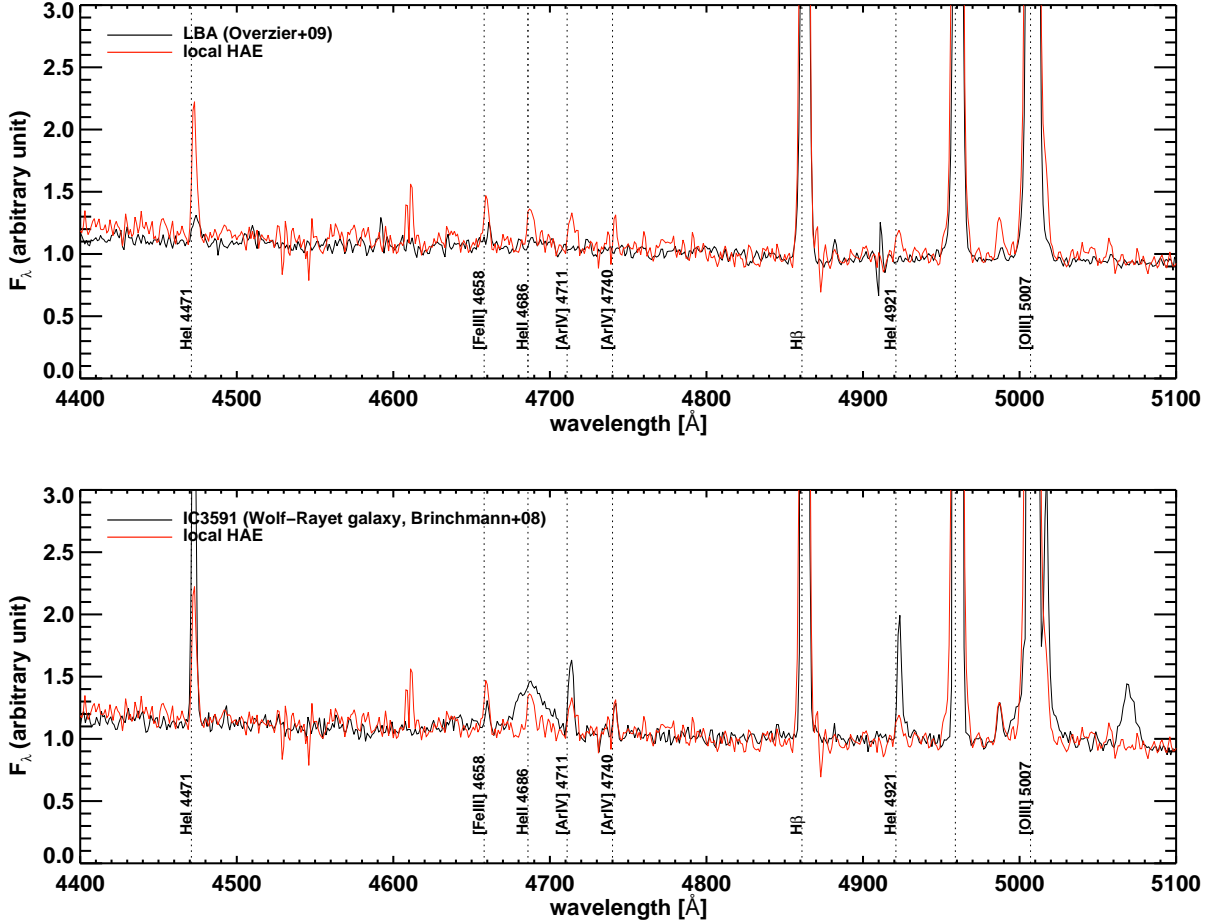


Fig. 4.— (*Top*): Comparison between the composite spectrum of 197 local HAEs that are not individually classified as Wolf-Rayet galaxies and the composite spectrum of 27 LBAs (Overzier et al. 2009). When making a composite spectrum, each spectrum was weighted using the continuum flux at 4800 Å and no evidence of spectral features indicating the existence of Wolf-Rayet stars (such as blue bump around HeII 4686 Å and/or HeII 4686 Å line itself) can be seen in each of the individual spectrum.. The composite spectrum of HAEs show HeII 4686 Å line which is a distinguishing characteristic of Wolf-Rayet galaxies. Moreover, other Helium lines and several metal lines at high ionization states including [FeIII] 4658 Å, [ArIV] 4771 Å, 4740 Å appear in the composite spectrum of local HAEs. (*Bottom*): Comparison between the composite spectrum of 197 local HAEs (same as above) and the spectrum of a single Wolf-Rayet galaxy IC3591 (chosen from Brinchmann et al. 2008; with H β EW of 263 Å). The composite spectrum of local HAEs show several emission lines similar to Wolf-Rayet galaxy, including He recombination lines and high-order Fe and Ar lines, although the composite spectrum lacks the broad “bump” around 4686 Å. However, the strength of emission lines appearing in this plot is more than 10 times lower in local HAEs than in Wolf-Rayet galaxies. In addition, among 299 local HAEs, 43 galaxies (14%) are individually identified as Wolf-Rayet galaxies in previous works for Wolf-Rayet galaxies (Zhang et al. 2007; Brinchmann et al. 2008b). This implies that the star forming environments in both the local HAE and Wolf-Rayet galaxies are similar.

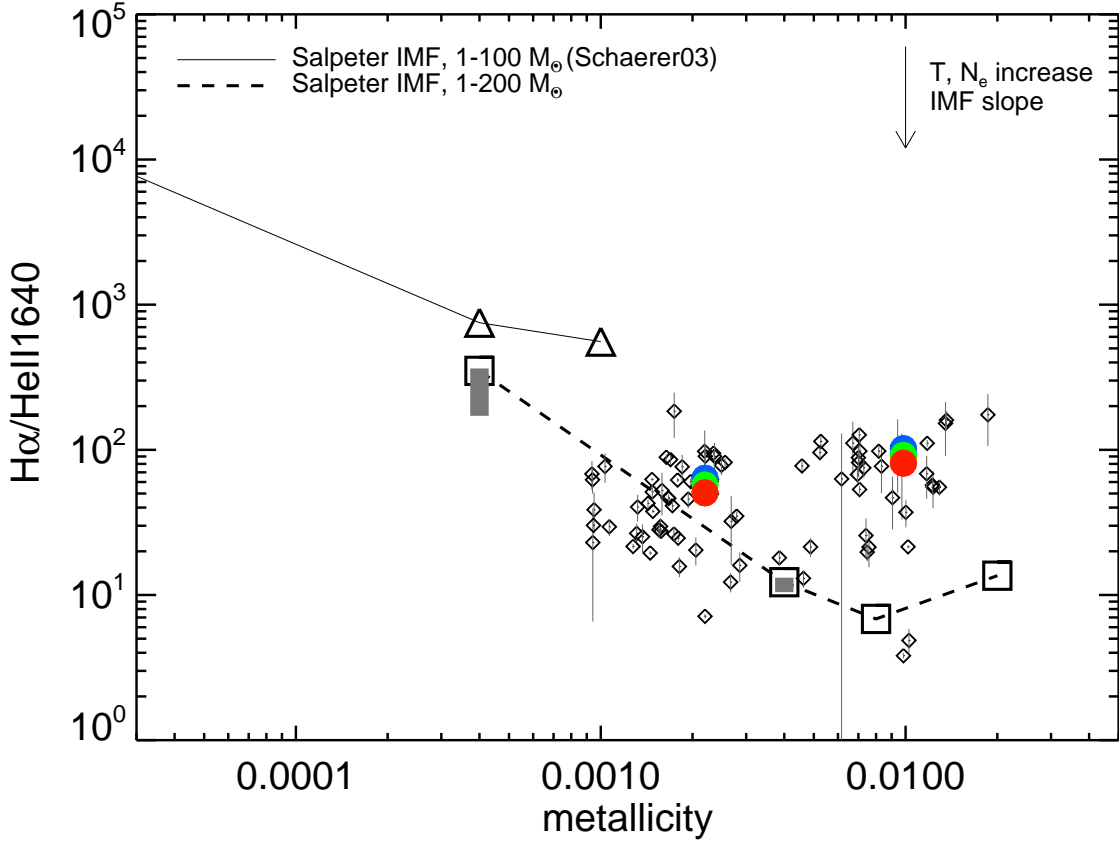


Fig. 5.— $H\alpha$ -to-HeII 1640 Å line flux ratio of local HAEs. $H\alpha$ line flux is measured from the SDSS spectrum, while the HeII 1640 Å line flux is estimated using the HeII 1640 Å/HeII 4686 Å ratio (Osterbrock & Ferland 2006) and the measured HeII 4686 Å line flux. We measured the HeII 4686 Å line flux using a simple Gaussian line profile fit. Diamonds are local HAEs with HeII 4686 Å detection in individual spectrum (including galaxies that are identified as Wolf-Rayet galaxies in Brinchmann et al. (2008b)). For local HAEs without individual HeII detection, not classified as Wolf-Rayet galaxies, we stacked their spectra and derived $H\alpha$ /HeII ratio from the stacked spectrum (filled circles). Circles with different colors show the possible range in $H\alpha$ /HeII ratio that can be spanned by changing the ionization temperature T and/or the electron density N_e . Overplotted as dashed and solid lines are expected $H\alpha$ /HeII ratio from the STARBURST99 population synthesis models (Leitherer et al. 1999; Schaerer et al. 2003). Thick gray rectangle shows the effect of changing the slope of the initial mass function on the $H\alpha$ /HeII line ratio; the slope has been changed from -0.4 (bottom) to -2.3 (top). The faint-end slope of the IMF, mass limit of the IMF, and the parameters regarding ionization environment (T , N_e) have relatively small effects on the observed $H\alpha$ /HeII ratio. On the other hand, metallicity appears to be the most dominant factor that affects the $H\alpha$ /HeII line flux ratio.

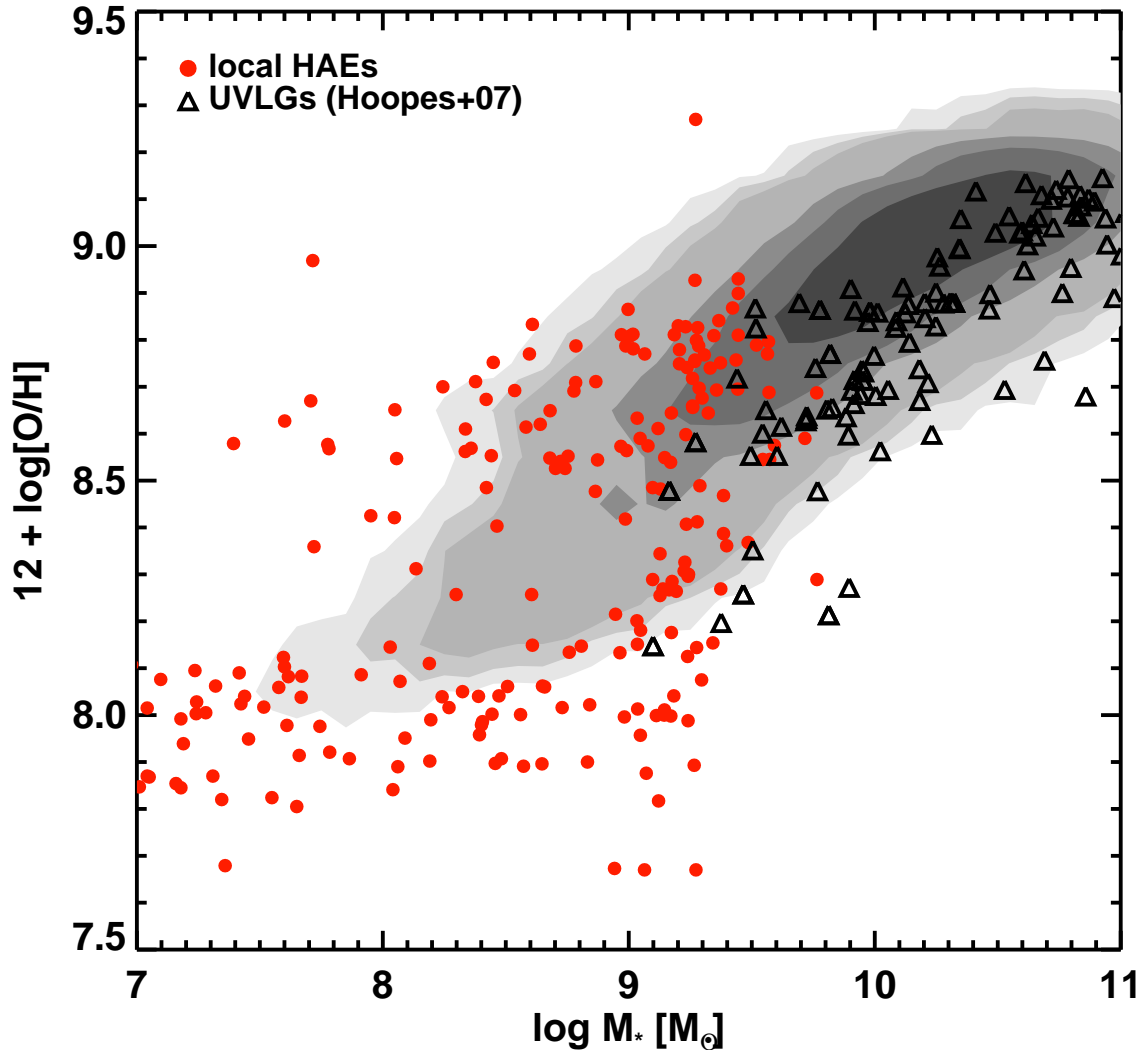


Fig. 6.— Mass-metallicity relation of the local HAEs (filled circles). Gas-phase metallicity and stellar mass for local HAEs are from the MPA-JHU value-added catalog constructed using SDSS DR7. Stellar mass has been derived based on photometry fits (methods from Kauffmann et al. 2003a; Salim et al. 2007) and gas-phase metallicity based on the emission line modeling (Tremonti et al. 2004; Brinchmann et al. 2004). Local HAEs are plotted over the contours which show the density distribution of entire SDSS DR7 galaxies that have been spectroscopically observed. Also compared here are UVLGs (triangles; Hoopes et al. 2007; $L_{FUV} > 10^{10.3} L_{\odot}$), among which the most compact galaxies are classified as LBAs. While half of the local HAEs are considered to be at the lowest end of metallicity distribution, most of the UVLGs are more metal-rich than local HAEs. In addition to metallicity, UVLGs are on average more massive than local HAEs. The difference between the two populations suggests that LBAs are possibly a “more evolved” galaxy population compared to HAEs.

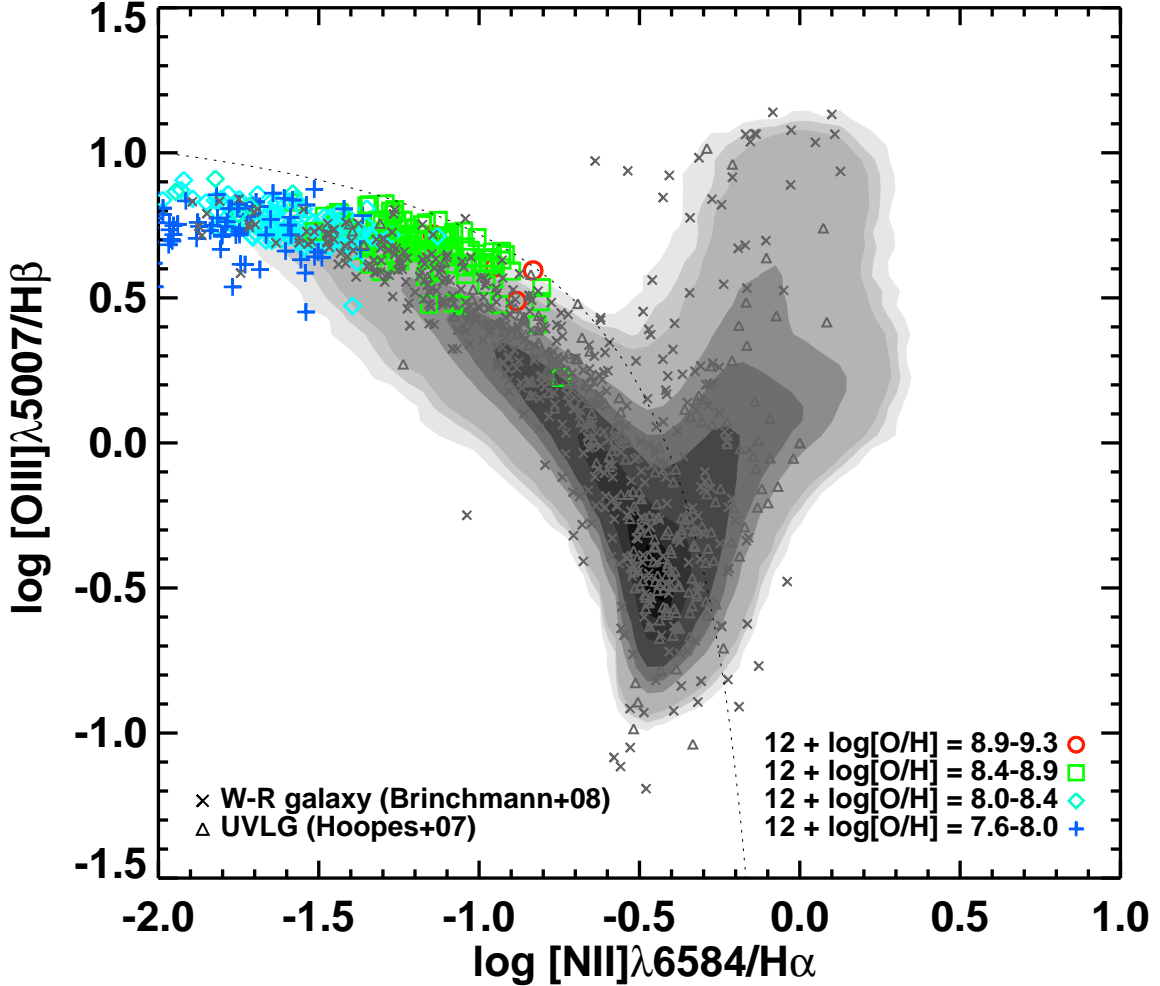


Fig. 7.— BPT diagram (Baldwin et al. 1981) of local HAEs. Contours show the density distribution of all emission line galaxies in the SDSS DR7. The dotted line represents the criterion that divides AGN-dominated galaxies (upper right) and star formation-dominated galaxies (lower left) as defined in Kauffmann et al.(2003b). Local HAEs with different gas-phase metallicities are plotted using different symbols: red circles correspond to most metal-rich galaxies ($8.9 < 12 + \log[\text{O}/\text{H}] < 9.3$) and the metallicity decreases as the symbol change to green squares, cyan diamonds, and blue crosses. It is clear that local HAEs are not AGN-dominated systems, especially due to their weak $[\text{NII}]\lambda 6584 \text{ \AA}$ emission. The $[\text{NII}]\lambda 6584 \text{ \AA}/\text{H}\alpha$ ratio is proportional to the gas-phase metallicity, thus the weak $[\text{NII}]\lambda 6584 \text{ \AA}$ of local HAEs indicate that these are metal-poor systems. Also shown are the locations of Wolf-Rayet galaxies (Xs; Brinchmann et al. 2008) and UVLG-LBAs (triangles; Hoopes et al. 2007) in the BPT diagram. Unlike the HAEs, Wolf-Rayet galaxies and the UVLGs do contain AGN dominated systems.

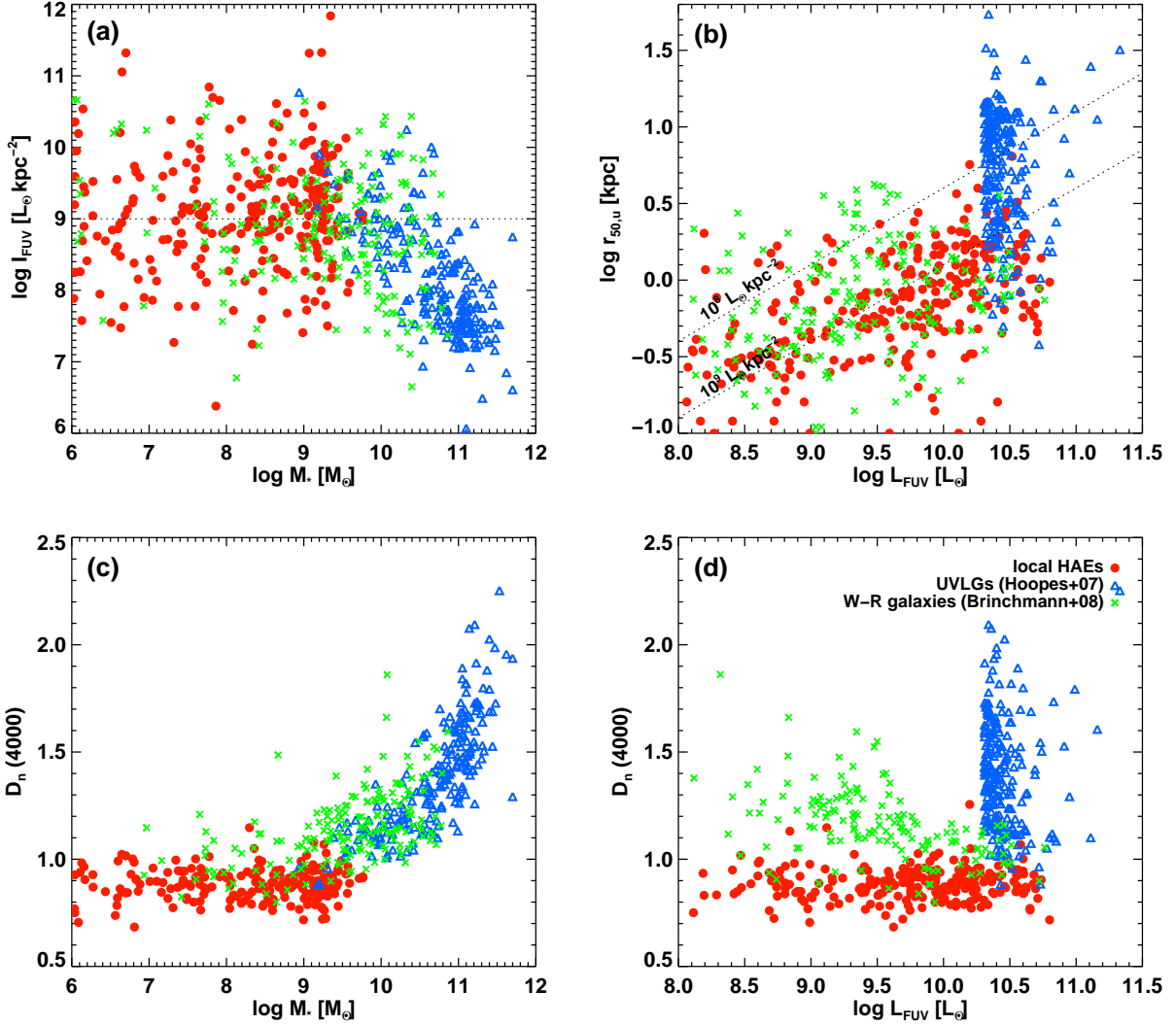


Fig. 8.— (a) FUV surface luminosity density (at 1500 \AA) vs. stellar mass for local HAEs (filled circles), UVLGs (triangles; Hoopes et al. 2007), and Wolf-Rayet galaxies (crosses; Brinchmann et al. 2008b). Dotted horizontal line at $I_{FUV} = 10^9 L_{\odot} \text{kpc}^{-2}$ indicates the criteria with which compact UVLG (LBA; Overzier et al. 2009) and non-compact UVLG are divided. UVLGs are the most massive among the three populations, although the FUV surface luminosity of HAEs and Wolf-Rayet galaxies are as high as that of UVLGs. (b) Half-light radius in SDSS u -band ($r_{50,u}$) and FUV luminosity of local HAEs, UVLGs, and Wolf-Rayet galaxies. Dotted lines indicate FUV surface luminosity density of $10^8, 10^9 L_{\odot} \text{kpc}^{-2}$ (y -axis in Figure 8a). Since the half-light radius is determined through exponential disk-fitting on the seeing-limited Sloan images, some ‘unresolved’ local HAEs are interpreted to have unreliably small half-light radius which are less than 100 pc. (c) 4000 \AA break strengths ($D_n(4000)$) and stellar mass of local HAEs, UVLGs, and Wolf-Rayet galaxies. It is clear that UVLGs are more evolved galaxy populations than HAEs, while HAEs are considered to be much younger from their low $D_n(4000)$. (d) 4000 \AA break strengths and FUV luminosity of local HAEs, UVLGs, and Wolf-Rayet galaxies. Wolf-Rayet galaxies and HAEs show similar FUV luminosity, galaxy size, and thus FUV surface luminosity which is also consistent with that of high-redshift star-forming galaxies. This suggests that the environment of star forming regions of these two galaxy populations is consistent with each other. However, two galaxy populations show differences in $D_n(4000)$ and stellar mass. The $D_n(4000)$ of Wolf-Rayet galaxies is not as homogeneously small as HAEs and HAEs are slightly less massive than Wolf-Rayet galaxies. Therefore, it is possible that there exists an evolutionary link between two population: Wolf-Rayet galaxies and HAEs share the same star formation environments, while HAEs are earlier stage of Wolf-Rayet galaxies before the evolution of metallicity and stars that enhance the 4000 \AA break.

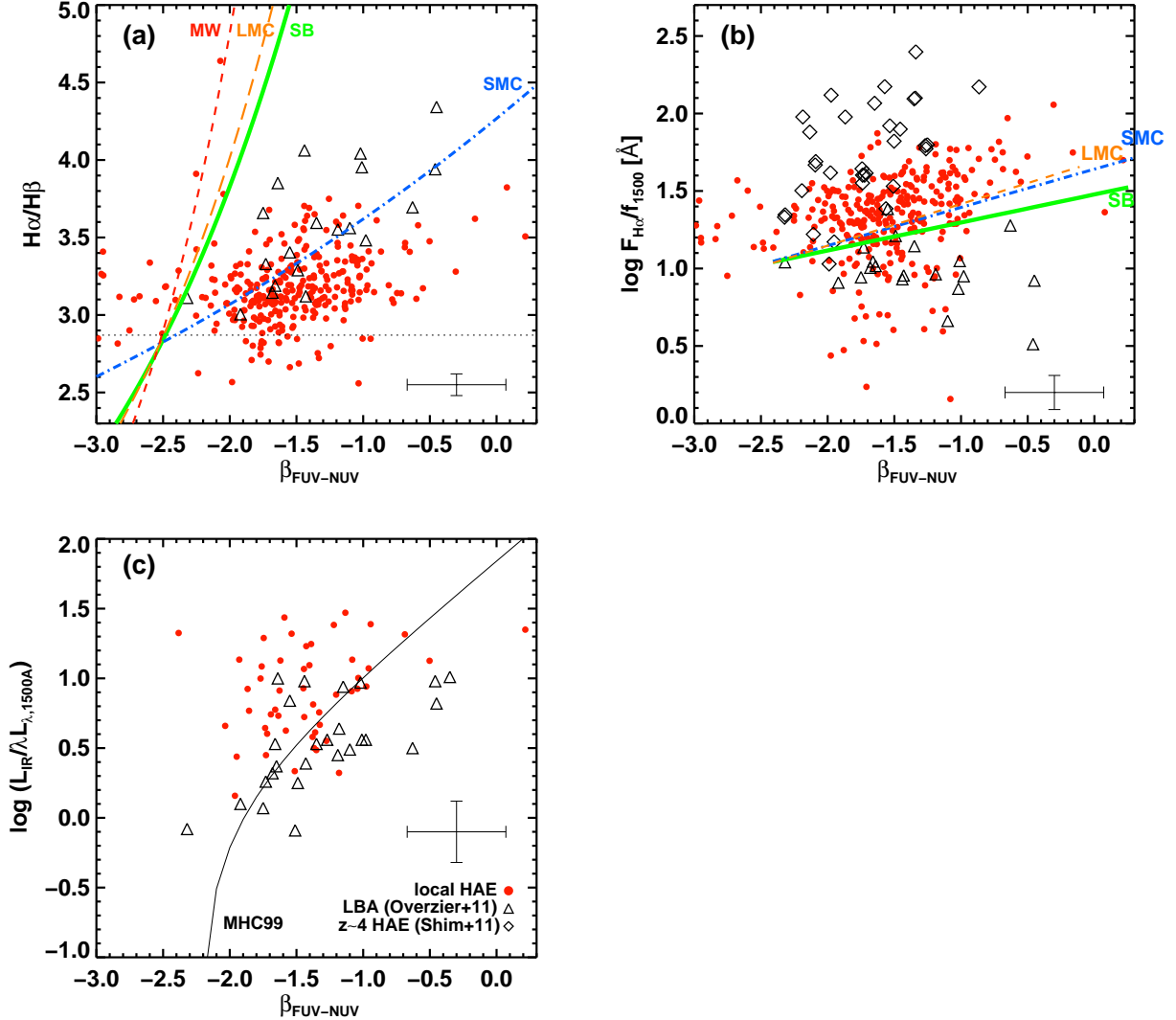


Fig. 9.— (a) Balmer line ratio ($H\alpha/H\beta$) vs. UV spectral slope β of local HAEs (filled circles) and LBAs (triangles; Overzier et al. 2011). UV slope β is derived using the GALEX FUV-NUV colors (see text for details), and $H\alpha/H\beta$ ratio are derived from the MPA-JHU catalog. Dotted horizontal line indicates $F_{H\alpha}/F_{H\beta} = 2.87$, the unobscured Balmer line flux ratio for case-B recombination with $T = 10^4$ K (Osterbrock & Ferland 2006). Overplotted tracks indicate $H\alpha/H\beta$ vs. β expected from different dust extinction laws (Allen 1976; Fitzpatrick 1986; Prevot et al. 1984; Calzetti et al. 2000). $H\alpha/H\beta$ ratio of local HAEs is difficult to explain using the SB extinction law: extinction laws with a steeper shape at UV wavelengths (e.g., SMC extinction law) is necessary. Some of the LBAs can be described using a SB extinction law with varying star formation history, but an SMC-like extinction law is required for some of the LBAs. (b) $H\alpha$ line-to-UV continuum flux ratio vs. UV spectral slope β of local HAEs (filled circles), LBAs (triangles), and $z \sim 4$ HAEs (diamonds; Shim et al. 2011). Here, f_{1500} indicates f_λ at 1500 Å. Overplotted lines indicate the relation between $H\alpha$ line-to-UV continuum flux ratio and β assuming different extinction laws, which could be shifted along the y-axis according to the star formation history assumed. However, $H\alpha/UV$ ratio is affected by both extinction and stellar population age, thus it is not as effective as the $H\alpha/H\beta$ ratio as a probe of different extinction laws among galaxies. Again in this plot, we see that there is almost no overlap between $z \sim 4$ HAEs and LBAs. (c) IR-to-UV luminosity ratio vs. UV spectral slope β of local HAEs and LBAs. Overplotted line shows the empirical IR-to-UV ratio vs. β relationship for local starbursts (Meurer, Heckman, & Calzetti 1999). Considering that HAEs are young galaxies and LBAs are more likely to be evolved systems, the IR/UV ratio of LBAs are expected to be smaller than that of HAEs since the fraction of stellar radiation that is absorbed by dust and re-radiated in IR decreases as the galaxy evolves. The observed IR/UV ratio confirms this idea, showing that most HAEs have higher IR/UV ratio than LBAs or other local star-forming galaxies (line from MHC 1999).